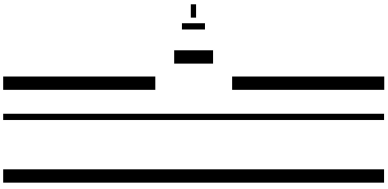

Westfälische
Wilhelms-Universität
Münster

Diplomarbeit

Gain Calibration of ALICE TRD Modules Using Cosmic Ray Data

vorgelegt von

Björn Albrecht

– Februar 2010 –

Contents

1 Introduction

After 2 decades of planning and construction and with costs of more than 3 billion euros, the Large Hadron Collider (LHC) started regular operations in November 2009. Being the latest facility at the European Organisation for Nuclear Research (CERN) in Geneva, its purpose is to find answers to the question:

"What is matter made of, and where does it come from?"

Already in 400 B.C. Democritus tried to answer this question and postulated that matter consists of indivisible particles which he named *atoms*. It took to the beginning of the 20^{th} century until scientists finally confirmed that matter is indeed made of such atoms. In the middle of the last century, looking deeper and deeper into the atoms, people like E. Rutherford or J. Chadwick discovered that atoms have a substructure of a nucleus of protons and neutrons in the centre, and a shell of electrons. Later, in the 1960s, M. Gell-Mann and G. Zweig developed mathematical theories in which protons and neutrons are made of even smaller objects they named *quarks*, although these quarks would have no physical reality. But then, R. Feynman analyzed high-energy particle collisions and proved protons and neutrons to have indeed a substructure of scattering particles he called *partons*. Later on, these partons were identified as quarks, which are nowadays considered to be the basic constituents of matter in the universe. Today, science has reached a state which makes it necessary to build such a big and complex machine as the LHC in order to investigate the composition of matter in even more detail.

A Large Ion Collider Experiment (ALICE) is one of six experiments installed at the LHC. The purpose of ALICE is to investigate the so-called *quark-gluon plasma* (QGP). Usually, quarks are bound in nuclear matter. But under such extreme conditions as have prevailed right after the Big Bang, theories predict that nuclear matter had undergone a phase transition to a QGP, where quarks can move as free particles. At the LHC, our aim is to generate the same extreme conditions by colliding lead ions at very high energies. Therefore, ALICE will be able to look back to the beginning of the universe.

ALICE comprises a set of subdetectors, one is the Transition Radiation Detector (TRD) which is assembled and tested at the Institute of Nuclear Physics in Münster. The TRD is subdivided into 540 independent multi-wire proportional chambers, grouped into supermodules of 30 chambers. For correct particle identification, a charged particle with a given momentum should generate the same signal in every chamber, but the signal amplification, the so-called *gain*, is not uniform within the TRD. Differences in gain are determined mainly by differences in the gas amplification of the chambers. The gas amplification gives the number of electrons that are detected after a particle has crossed the detector and ionized gas atoms in there. Furthermore, differences in the amplification of the readout electronics of the TRD also influence the gain.
In this thesis, local differences in gain inside the TRD supermodules were investigated. Considering different gain factors, the TRD chambers can be calibrated to a uniform signal amplification. In addition, the dependence of the gain on the applied voltage and pressure was studied.

The following chapter gives a short overview on the theoretical background of ALICE. Chapter 3 describes ALICE and the LHC in general, the TRD is described in more detail in chapter 4. In chapter 5, a general introduction to gain in multi-wire proportional chambers is given, the experimental setup is explained in chapter 6. The calibration procedure is presented in chapter 7. Chapter 8 presents results from tests of the calibration software. The analyses on gain calibration of the TRD can be found in chapter 9. After this, the results are summarized in chapter 10.

2 Theoretical Background

This chapter intends to give the reader a short summary of the models needed to be known in order to understand the purpose of the ALICE experiment.

2.1 Basic Constituents of Matter

The visible matter in the universe consists of atoms, which can be considered as the elementary particles of chemistry. Until the end of the 19^{th} century, over 80 elements were discovered, where each element is a different type of atom. The atoms were considered as indivisible, until the discovery of radioactivity disproved this assumption in the early 20^{th} century. Even before that, E. Rutherford discovered that the atom itself has a substructure, it is composed of a negatively charged shell and a positively charged nucleus. In a simple model according to N. Bor, the nucleus is fixed in the centre of the atom and the shell is filled with a number of electrons orbiting the nucleus.
Nearly all the volume of an atom is empty space, because the nucleus is about 10,000 times smaller than the atom (typical diameters are 10^{-10} m for the atom and 10^{-14} m for the nucleus), and the nucleus carries over 99.9 % of the atomic mass.
The nucleus itself is composed of two types of even smaller particles, the *proton* (p) and the *neutron* (n). Later on, scientists looked deeper[1] into protons and neutrons, and discovered that they are composed of three quarks each: $p = (u, u, d)$ and $n = (u, d, d)$. According to the standard model (see section 2.2), quarks are point-like particles and are considered as the basic constituents of matter today.
During the last 60 years, many more particles containing quarks have been found in accelerator experiments. All of them are either composed of three quarks (qqq), three anti-quarks ($\bar{q}\bar{q}\bar{q}$), or a pair of quark and anti-quark ($q\bar{q}$). Particles containing three quarks are called *baryons*, the ($q\bar{q}$)- pairs are called *mesons*. Baryons and mesons together were named *hadrons*.
All of these discovered particles are unstable, as free particles as well as in bound states like the atomic nucleus.

[1] Using deep inelastic scattering with leptons.

2.2 The Standard Model of Particle Physics

The theory called the standard model of particle physics includes all particles which have been detected until today, and it describes all kinds of interaction between these particles, except for the gravitation. It also describes a few more particles that have not been found yet, e.g. the graviton.
According to this model, all matter consists of spin-$\frac{1}{2}$ particles called *fermions*. The fermions are subdivided into leptons and quarks. The leptons consist of the *electron*, *muon* and *tau*, and the related *neutrinos* ν_e, ν_μ and ν_τ. The six quarks are called *up*, *down*, *charm*, *strange*, *top* and *bottom*, carrying an additional colour charge.
All fermions are separated into three generations, corresponding to their masses, and therefore the energies at where they can be created. Some properties of fermions are summarized in table 2.1.

Fermions	Generation	Name	El. Charge	Mass
Quarks	1	u	2/3 e	1.5 - 3.3 MeV/c^2
		d	-1/3 e	3.5 - 6.0 MeV/c^2
	2	c	2/3 e	1.2 - 1.3 GeV/c^2
		s	-1/3 e	70 - 130 MeV/c^2
	3	t	2/3 e	169 - 173 GeV/c^2
		b	-1/3 e	4.1 - 4.4 GeV/c^2
Leptons	1	e^-	-e	0.511 MeV/c^2
		ν_e	0	$\leq$ 2 eV
	2	μ	-e	105 MeV/c^2
		ν_μ	0	$\leq$0.19 MeV/c^2
	3	τ	-e	1.78 GeV/c^2
		ν_τ	0	$\leq$ 18.2 MeV/c^2

Table 2.1: Properties of quarks and leptons in the standard model [eaPDG09].

In the world of particle physics, alongside matter, there is always anti-matter created as well. It takes twelve fermions to form all matter. Each of these fermions has an anti-particle to form all anti-matter, so there are 24 basic constituents of matter.

Four interactions, also called the four fundamental forces, act on fermions. The strong interaction, the weak interaction, the electromagnetic interaction and the gravitation. The first three of them are described by the standard model. In this model, all interactions are mediated via particles of integer spin called gauge *bosons*. In order to mediate a force, a boson has to couple to a fermion. It can only couple if the fermion carries a charge corresponding to the applied interaction.

The strong interaction is mediated via 8 different *gluons* that couple to colour charged particles. Quarks are the only fermions carrying a colour, "red", "green", "blue", or one of the corresponding anti-colours. Therefore leptons do not take part in the strong interaction. The gluons on the other hand carry colour charge and are subject to the strong interaction themselves. As a consequence, the strong interaction does only have a very short range of ~ 1 fm, the size of a proton. Due to this force, atomic nuclei as well as their constituents, the protons and neutrons, are held together.
The weak interaction can change the "flavour" of a fermion, e.g. transform an up-quark into a down-quark, and is for example responsible for the β-decay. All fermions carry a weak charge and take part in this interaction. The bosons mediating the weak force are W^+, W^- and Z^0. Because of their large masses, the range of ~ 1 pm is the smallest of all interactions.
The electromagnetic interaction is mediated via a *photon* (γ). It couples to electrically charged particles, i.e. all fermions except for the neutrinos (ν_e,ν_μ,ν_τ). The photon has no rest mass and no charge, therefore the electromagnetic force is of infinite range.

The table 2.2 gives an overview on these three interactions. In terms of the standard model, the gravitation applies to all particles carrying mass, its range is infinite, and it should be mediated via a boson called graviton, though this is only postulated but not found yet.

Force	Range (m)	Gauge Boson	Mass (GeV/c^2)	Couples to
Strong nuclear	10^{-15}	8 Gluons (g)	0	colour
Weak nuclear	10^{-18}	$W^\pm$, Z^0	$\approx 10^2$	weak charge
Electromagnetic	∞	Photon (γ)	0	electric charge

Table 2.2: The fundamental forces as described by the standard model. The gravitation as the 4^{th} fundamental force is still missing in this model [P+06].

2.3 The Quark-Gluon Plasma

Looking at section 2.1 one recognizes that quarks, being the elementary particles of matter, are never observed as free, single quarks, but only in bound hadronic states. This is due to the nature of strong interaction.
As described in section 2.2, strong interaction is mediated by gluons, coupling to colour charge and carrying colour themselves. Therefore the gluons are strongly interacting with each other. As a consequence, the strong force becomes infinitely

large on large ranges ($\gg 1$ fm) and vanishes for small ranges. So a quark can never leave a hadron, this is called *confinement*. The effect of vanishing force on small ranges is called *asymptotic freedom*.
The underlying theory of strong interaction is the Quantum Chromodynamics (QCD). Solving the QCD equations on a numerical lattice, scientists realized that for extremely high energy densities (given at extremely high temperatures and/or pressures), the quarks become deconfined, meaning there should be free quarks and gluons in nuclear matter. A new state of matter was proposed, a quark-gluon plasma (QGP).
Introducing the bag model for hadronic matter, a simple model assuming quarks in hadrons to be massless objects separated from the outside QCD vacuum in a bag, solving the equations of that model for a QGP gave an astonishing result: It should be possible to describe this new state of matter in terms of thermodynamical variables such as temperature, pressure, entropy, etc. [YHM05]. One can even plot a phase diagram for the QGP as shown in figure 2.1. The baryochemical potential μ_B on the x-axis is a measure for the net baryon density ϱ, the difference between baryon and anti-baryon number, which scales with the pressure. So μ_B is an indirect measure for the pressure. The phase border is subdivided into different parts: The solid line indicates a first-order phase transition, at which the system absorbs energy without an increase of temperature[2]. The circle gives the critical end point of this first-order phase transition [Nol05]. The dashed line indicates a possible crossover region, where the phase transition is rapid and continuous. The existence of this crossover region, as well as the position of the critical point, are model dependent and still not well estimated. The ALICE experiment will investigate nuclear matter for vanishing density at $\mu_B \approx 0$. The critical temperature to form a QGP at zero density is predicted to be $173\,\mathrm{MeV} \pm 10\ \%$ [BMS07]. In common units, this would be about $2 \cdot 10^{12}\,\mathrm{K}$, this is 100,000 times the temperature in the centre of the sun.
The critical energy density ε_c for a QGP phase transition should be $0.7 \pm 0.2\,\mathrm{GeV\,c^{-2}\,fm^{-3}}$. This is five times the energy density of nuclear matter [BMS07]. Another approach to this phase transition follows high densities, where ε_c can be reached at lower temperatures.
Since it takes such extreme conditions to form a QGP, it is assumed that if it exists in the universe today, it might only appear in the centre of neutron stars because of the large pressure in the core. But at the birth of the universe, from around 10 ps up to $10\,\mu$s after the Big Bang, the models predict that matter took the form of a QGP. Afterwards, while the universe rapidly cooled down, the quarks and gluons froze out and formed hadronic matter.

[2] Comparable to melting ice.

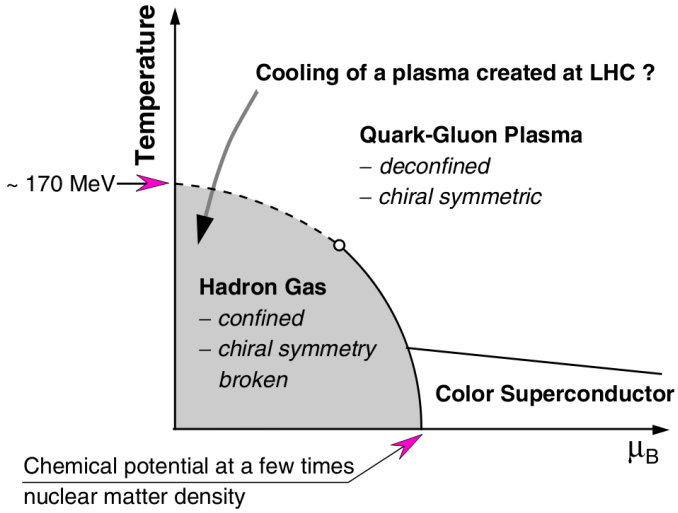

Figure 2.1: The phase diagram of QCD: The solid line indicates a first-order phase transition, the dashed line indicates a crossover transition. The circle in between is the critical end point of the first-order phase transition. The exact positions are not yet investigated [ALI04].

It is impossible to investigate matter under such astronomical scales in the laboratory, but fortunately there should be a third method to create a QGP: heavy-ion collisions. The next section will give a short summary on previous and future experiments on the quark-gluon plasma.

2.4 Experiments on the QGP

Collisions of heavy atomic nuclei, i.e. heavy ions, can create enough temperature or density to form a QGP. To talk of a QGP as a thermodynamical system, it has to be composed of a large number of particles, and secondly, it has to reach a local equilibrium. This means that every particle should undergo a sufficient number of collisions during the lifetime of the system. Colliding heavy nuclei like gold or lead at high energies should provide these conditions and allow the system to form for a short time of about 10^{-22} s a so called *fireball* of QGP matter. Figure 2.2 illustrates the QGP creation for a simulated collision between two nuclei: Panel 2.2 (a) shows the Lorentz contracted nuclei prior to the collision. In 2.2 (b) the nuclei collide and their components experience many collisions while the nuclei penetrate each other. Between the diverging fractions of the nuclei, in 2.2 (c) a fireball of QGP is generated. Afterwards, in panel 2.2 (d), the last inelastic scattering has taken place and all quarks have recombined to hadrons *(chemical freeze-out)*. Soon after elastic scattering stops, too *(thermal freeze-out)*.

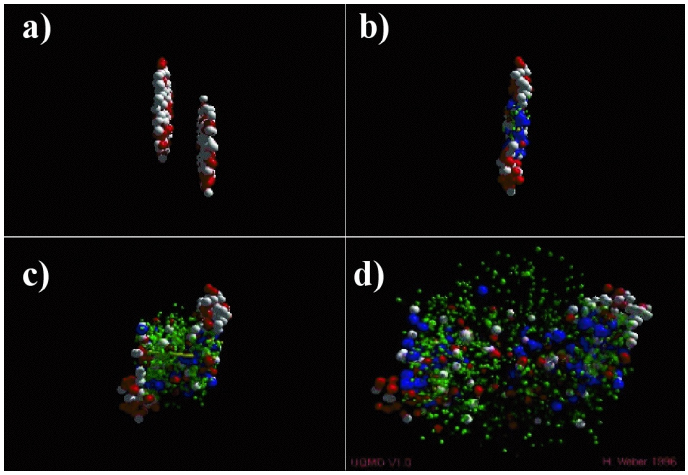

Figure 2.2: Simulation of QGP creation in the collision of two heavy nuclei. The nuclei appear as thin disks due to Lorentz contraction [Web96].

Since the early 1990s, experiments on heavy-ion collisions were made with two high energy accelerators: The Alternating Gradient Synchrotron (AGS) at BNL[3], and the Super Proton Synchrotron (SPS) at CERN[4] with centre-of-mass energies per colliding nucleon pair of $\sqrt{s_{NN}} = 4.6\,\text{GeV}$ and $\sqrt{s_{NN}} = 17.2\,\text{GeV}$, respectively. In 2000, the Relativistic Heavy-Ion Collider (RHIC) started operations at BNL, providing collision energies of $\sqrt{s_{NN}} = 200\,\text{GeV}$ for heavy-ion beams. At least for the NA50[5] experiment at SPS and the PHENIX[6] experiment at RHIC there is good evidence that a new state of matter has been created [A$^+$00], [A$^+$05]. Some QGP traces were also observed by other RHIC and SPS experiments [RHI05], [cer09a].
In 2008, the Large Hadron Collider (LHC) has started operations at CERN, where the ALICE experiment has the opportunity to survey Pb-Pb collisions with $\sqrt{s_{NN}} = 5.5\,\text{TeV}$. This energy should allow to examine for thermodynamical properties of the QGP.
In 2016, another experiment on QGP will start: The Compressed Baryonic Matter (CBM) experiment at the FAIR[7] accelerator at GSI[8]. While all former experiments survey matter for $\mu_B \approx 0$ and highest temperatures, CBM aims to create a QGP at high pressures. As a fixed target experiment, FAIR will provide beam energies up to 35 AGeV for U^{92+} [KB09].

[3]Brookhaven National Laboratory, Upton, New York
[4]European Organization for Nuclear Research, Geneva
[5]North Area experiment 50
[6]Pioneering High Energy Nuclear Interaction eXperiment
[7]Facility for Antiproton and Ion Research
[8]Gesellschaft für Schwerionenforschung, Darmstadt

2.5 Signatures of the QGP

With a lifetime of 10^{-22} s, the quark-gluon plasma in heavy-ion collisions is much shorter lived than after the Big Bang. This is due to the much lower energy in such experiments. As a consequence, it is impossible to observe a QGP directly. Instead, people are looking for certain traces in experimental data that a QGP should leave behind compared to ordinary hadronic matter. In addition, it is not sufficient to just measure a single signature, only a larger quantity of experimental observables can give strong evidence of the presence of a QGP. The most important signatures are given below.

J/Ψ Suppression
Colliding nuclei at high energies can produce matter as pairs of quark (q) and anti-quark ($\bar{q}$). Some of these ($q\bar{q}$)-pairs can form meta-stable bound states comparable to a positronium. The J/Ψ is a bound state of charm and anti-charm quark ($c\bar{c}$). In presence of a QGP, quarks and gluons are free to move, the c and $\bar{c}$ move independently through the fireball and are screened by the other quarks in between. At freeze-out it is unlikely for the ($c\bar{c}$)-pair to form a J/Ψ, instead each forms a D-meson with a neighbouring quark. So, the number of J/Ψ-particles should be suppressed compared to p-p collisions at the same energy [YHM05]. This suppression was already observed in Pb-Pb collisions, at the NA50 experiment at CERN-SPS and at the PHENIX experiment at RHIC [A$^+$00], [A$^+$05].
For LHC energies, a contrary behaviour is expected. Due to the much higher collision energy, many more ($c\bar{c}$)-pairs will be produced. At freeze-out there is a possibility that charm and anti-charm quarks from different origins are close enough to form a J/Ψ. Therefore an enhancement of J/Ψ production is expected for a QGP at LHC [ALI04], [BMS07].

Strangeness Enhancement
In the strong interaction, strangeness is conserved, consequently, in heavy-ion collisions strange quarks are created as ($s\bar{s}$)-pairs.
Without a QGP, the ($s\bar{s}$) quarks can only appear as components of strange mesons, most likely kaons, because single quarks cannot exist. The energy needed to produce two kaons is 987 MeV. Since kaons are the lightest strange mesons, it gives the threshold energy for creating strange quarks in hadronic matter.
Inside a QGP, ($s\bar{s}$)-pairs can be created directly with a threshold energy of 300 MeV, corresponding to their masses. Thus, the number of strange particles should increase in presence of a QGP [YHM05].

Jet Quenching
At an early stage in heavy-ion collisions, two scattered partons can have that much energy that a pair of high energetic quarks is produced. These two particles leave the collision point in opposite direction with large transverse momenta. Directly after the collision, each particle fragments into a cluster of hadrons, called a *jet*. The jets propagate in the same direction as their originating particle, under a relative angle of 180° in their centre-of-mass system. The creation of gluons and events with three jets are also possible.
In presence of a QGP, there should be a difference. In most cases, the hard parton-parton scattering takes place at the very beginning of the collision. So, one of the partons has to travel a longer distance through the strongly interacting fireball, where it loses much energy and might even be completely absorbed. Therefore, detected jets are expected to be attenuated and uncorrelated [YHM05], [ALI04].

Photons and Leptons
Since photons and leptons do not interact strongly, they can survive a whole process of fireball creation, thermal equilibrium and freeze-out unmodified. Prompt photons are emitted by the hard parton-parton scattering directly after the collision, thermal photons are emitted as black body radiation in the thermally equilibrated phase. Together, prompt and thermal photons are called direct photons. Direct photons are a good probe for the different stages of QGP creation.
Leptons are created in heavy-ion collisions, too. For example, a J/Ψ can decay into a pair of e^-e^+. Compared to photons, these lepton pairs carry an additional variable, the pair invariant mass, useful to investigate excited states of matter [ALI04].

Anisotropy of Momentum
It turns out that a QGP can be described in terms of hydrodynamic models. In fact, the evolving fireball can be regarded as a perfect fluid. For collisions with impact parameter $b \neq 0$, i.e. no direct head-to-head collisions, the overlap region of the two colliding nuclei is anisotropic and a pressure gradient with respect to the interaction plane is induced. If the energy is sufficiently high and thermalization is reached at an early stage of the collision, the space anisotropy results in an anisotropy of the scattered particles momenta: the elliptically shaped fireball bursts outwards, fastest in beam direction, so after hadronizing the particles momenta will be anisotropic in angle. This is called *elliptic flow* [ALI04], [WKB09]. Such a behaviour has already been observed at RHIC, in 2000 at the STAR[9] experiment, and in 2002 at the PHENIX experiment [A$^+$01], [A$^+$02].

[9]Solenoidal Tracker at RHIC

3 ALICE and the LHC

3.1 Large Hadron Collider (LHC)

The Large Hadron Collider (LHC) is a particle accelerator at CERN, and it is one of the biggest machines ever built. Starting first operations in mid 2008, it is dedicated to accelerate protons as well as lead ions close to the speed of light c (0.999999991 c for protons). In the LHC, two beam tubes are routed in a ring tunnel of ~ 27 km circumference. In both tubes charged particles are accelerated, but in opposite directions. The tunnel lies about 100 m below ground in the area of Geneva, partly in Switzerland and partly in France. See figure 3.1 for an overview. Across the ring, eight arches are distributed, each with 154 dipole magnets to bend the beams. For each tube, there are eight radiofrequency cavities to accelerate and focus the beam. Focusing is also done by additional quadropole magnets between the arches. On the whole, there are 9593 magnets installed at the LHC. In order to achieve the high magnetic fields needed to bend the beam (that is 8.3 T for the dipole magnets) these magnets are built out of superconducting coils, running at a temperature of 1.5 K. At this temperature, a current of 11700 A can flow in the coils without resistance. Most magnets are cooled down by liquid helium, thus the LHC is the biggest cryogenic system on earth [CER08].

After having passed a setup of pre-accelerators, the particles are injected in the LHC and accelerated up to centre-of-mass energies of $\sqrt{s} = 14$ TeV for proton-proton collisions and $\sqrt{s_{NN}} = 5.5$ TeV for Pb-Pb collisions. For heavy-ions, this is about 30 times the energy of RHIC (see 2.4). The beams are discontinuous and composed of *bunches* of particles. Heavy-ion beams will contain 592 bunches, each composed of 10^7 ions [Zim09].
At four interaction points, the bunches collide with a luminosity[10] of $10^{34}\,\mathrm{cm}^{-2}\mathrm{s}^{-1}$ for protons and $10^{27}\,\mathrm{cm}^{-2}\mathrm{s}^{-1}$ for lead nuclei [CER08], [CER95]. At the interaction points, large underground caverns are installed with the four main LHC experiments:

[10] The luminosity L gives the number of particles per second, crossing an area of $1\,\mathrm{cm}^2$ at the interaction point.

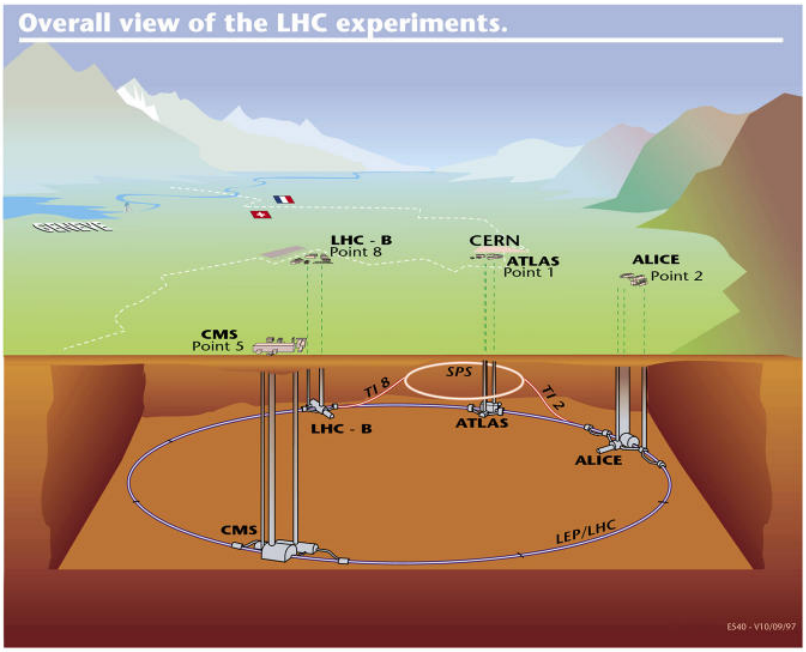

Figure 3.1: Schematic view on the LHC and the related experiments [CER09b].

ATLAS[11] and CMS[12] are both designed to study the same amount of particles, but were built independently of each other which provides a cross-check of results. Their major aim is to discover the higgs particle, a boson supposed to give particles their masses [CER08]. Furthermore, these two experiments search for supersymmetric particles and extra dimensions, both predicted by extensions of the standard model. LHCb[13] will investigate CP-violation in interactions of particles containing b-quarks. It aims to explain the reason for the asymmetry between matter and anti-matter in the universe. These three experiments will survey mainly p-p collisions.
ALICE[14] will study Pb-Pb collisions. It intends to survey the properties of the quark-gluon plasma. The ALICE experiment is subject of this thesis and will be explained in more detail in section 3.2.
Two smaller, more specific experiments are implemented alongside the four major experiments. Both investigate *forward particles*, these are particles out of the bunches that were only slightly deflected in the collision. LHCf[15], placed near ATLAS, aims to confirm models on ultra high-energy cosmic rays. TOTEM[16], placed

[11] A Toroidal LHC ApparatuS
[12] Compact Muon Solenoid
[13] Large Hadron Collider beauty experiment
[14] A Large Ion Collider Experiment
[15] Large Hadron Collider forward
[16] Total Cross Section, Elastic Scattering and Diffraction Dissociation

near CMS, will provide information on the LHC itself, e.g. total cross-section and luminosity [CER08].

3.2 ALICE - A Large Ion Collider Experiment

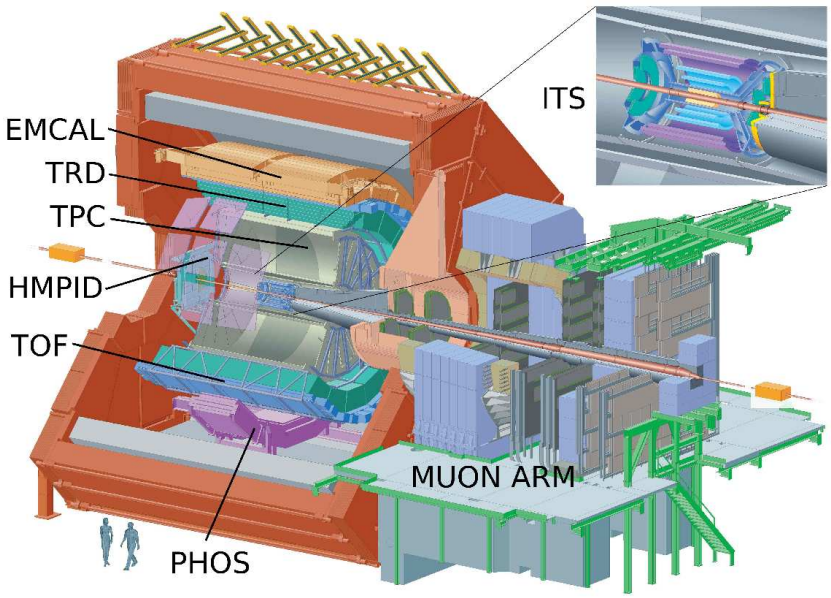

Figure 3.2: The central barrel detectors of the ALICE experiment and the muon arm [Wul09], based on [ALI04].

A Large Ion Collider Experiment (ALICE) is a general purpose, heavy-ion detector at CERN. It is dedicated to explore the phase transition between nuclear matter and a QGP at $\mu_B = 0$ in Pb-Pb collisions. Besides, physics runs with p-p collision will be recorded, too, in order to compare the results to heavy-ion data. With a size of $16 \times 16 \times 26\,\mathrm{m}^3$, it weighs about $10,000\,\mathrm{t}$. It is able to detect and identify a broad range of particles (different hadrons, electrons, muons and photons) produced in nucleus-nucleus collisions, reconstruct their vertices and measure their energies.
The ALICE experiment can be subdivided into a central barrel part, located around mid-rapidity ($\eta = 0$)[17] with respect to the collision point, and a Muon Arm and other forward detectors under smaller angles relative to the beam. Figure 3.2 shows the setup. The central barrel detectors are installed inside a big solenoid magnet

[17]The pseudorapidity $\eta = \frac{1}{2}\ln\left(\frac{|\vec{p}|+p_z}{|\vec{p}|-p_z}\right)$ of a particle is a measure for its angle relative to the beam direction. In ultra-relativistic collider experiments like ALICE, it is $\eta = -\ln\left(\tan(\frac{\Theta}{2})\right)$.

named L3, working at room temperature. It provides a homogeneous magnetic field of 0.5 T. Charged particles travelling through that field are deflected due to the Lorentz force, hence their charge and momentum can be reconstructed. In the central barrel, the tracking subdetectors of ALICE cover an Θ-angle of 45° to 135°, corresponding to a pseudorapidity of $|\eta| \leq 0.9$, and the total azimuth. Starting at the collision point and moving outwards, these detectors are the following:
The beam pipe of 6 cm diameter is surrounded by the Inner Tracking System (ITS). This system consists of different types of silicon detectors. Its main purpose is to resolve decay vertices of particles containing c-, b-, or s-quarks. Furthermore, together with the TPC data, it can improve the tracking. The Time Projection Chamber (TPC) is the main tracking device in ALICE. It provides charged particle momentum measurement with a good two-track separation. In addition, it is used for *Particle Identification* (PID). Next comes the Transition Radiation Detector (TRD). Its main purpose is to distinguish electrons from pions. Alongside PID, it serves as a fast trigger and improves the ITS and TPC tracking. Since the experiments in this thesis were done with TRD supermodules, the TRD is described in more detail in chapter 4. More outwards, the Time Of Flight (TOF) detector is installed. It measures the time it takes a particle to travel from the interaction point to the surface of the detector with a time resolution better than 100 ps. Together with information on the track positions, the time information from TOF is used for PID. The detectors presented so far cover a range of $|\eta| \leq 0.9$ and the full azimuth of $\varphi = 360°$. The High-Momentum Particle Identification Detector (HMPID) is dedicated to improve the PID for high momentum particles with $p_t > 1\,\mathrm{GeV/c}$[18]. With $|\eta| < 0.6$ and $1.2° < \varphi < 58.8°$, it covers a smaller range. More outwards, two electromagnetic calorimeters are installed. The Photon Spectrometer (PHOS) is positioned at the bottom of the ALICE setup with an azimuth angle of $\Delta\varphi \approx 100°$ and $|\eta| < 0.12$. The main goal of PHOS is to test thermal and dynamic properties of the initial phase of the collision by measuring energies of direct photons. The Electromagnetic Calorimeter (EMCal) lies approximately opposite to PHOS, covering $\Delta\varphi \approx 107°$ and $|\eta| < 0.7$. Where PHOS provides higher resolution, the EMCal provides larger acceptance for high p_t photons and hadrons in order to study jet fragmentation.
Outside the L3 magnet, at $-4.0 < \eta < -2.5$, stands the Muon Spectrometer. It consists of a subset of different detectors and components. Heavy-quark vector meson resonances, e.g. the J/Ψ, can be measured via their $\mu^+\mu^-$-decays.
In addition, a couple of smaller, more specialized detectors are installed in forward direction on both sides of the central barrel.
It is to say that at the beginning of 2010, not all previously described detectors

[18]The transverse momentum $\vec{p_t}$ of a particle gives the part of its momentum perpendicular to the beam direction.

are completely installed. For more information on the ALICE experiment and the functionality of its subdetectors see [ALI08], [ALI04].

4 The TRD in ALICE

The charged particles produced in heavy-ion collisions comprise a large number of pions. It is most likely for massive particles to hadronize into pions, because they are the lightest hadrons. On the other hand, in order to measure the production of light and heavy vector-mesons, semi-leptonic decays with open charm and open beauty and correlations in production of these hadrons, it is important to identify the electrons in this large background of pions. Therefore, the Transition Radiation Detector (TRD) has been developed and added to the ALICE setup. It is designed to reconstruct tracks of charged particles, measure their energy deposit in the detector and most importantly, distinguish electrons from pions. The pion suppression should reach a factor better than 100 for particles with $p_t > 3\,\mathrm{GeV/c}$ [ALI01].
In addition, it serves as a fast trigger on high p_t particles and electrons in order to study for example J/Ψ decays. The trigger decision is available about $6\,\mu$s after the collision.

4.1 TRD Setup

Located between TPC and TOF, the TRD will be installed into a mechanically supporting structure named *spaceframe*. The TRD covers a pseudorapidity range of $|\eta| \leq 0.9$ and an azimuth $\varphi = 360°$. In radial direction it is located between $2.9\,\mathrm{m} \leq r \leq 3.7\,\mathrm{m}$ from the beam axis [ALI01]. The detector is assembled and installed as 18 individual *supermodules*, each covering an azimuth segment of 20°. Along with mechanical stability, the supermodule frames provide power supply and cooling for the readout electronics. Each supermodule (SM) contains 30 detector chambers, arranged in stacks and layers. In beam direction (z-axis), the SMs are subdivided into 5 stacks, each with 6 layers of chambers in radial direction. For the cylindrical coordinates of the TRD, the chambers are of different size. There are two types of chambers, C0 and C1. The C0 chambers are installed in stack 2, exactly in the middle of the TRD at $\eta = 0$. They have the same length in all layers. The other stacks are filled with C1 chambers. The further outwards the layer, the longer the C1 chambers are in z-direction as well as in φ-direction [ALI01].

In total, the TRD will consist of 540 chambers[19]. The chamber coordinates (x, y, z) are related to the global TRD coordinates (r, φ, z) in the following way: x corresponds to r, y corresponds to negative φ. Chamber z is the same as global z. Figure 4.1 illustrates the configuration.

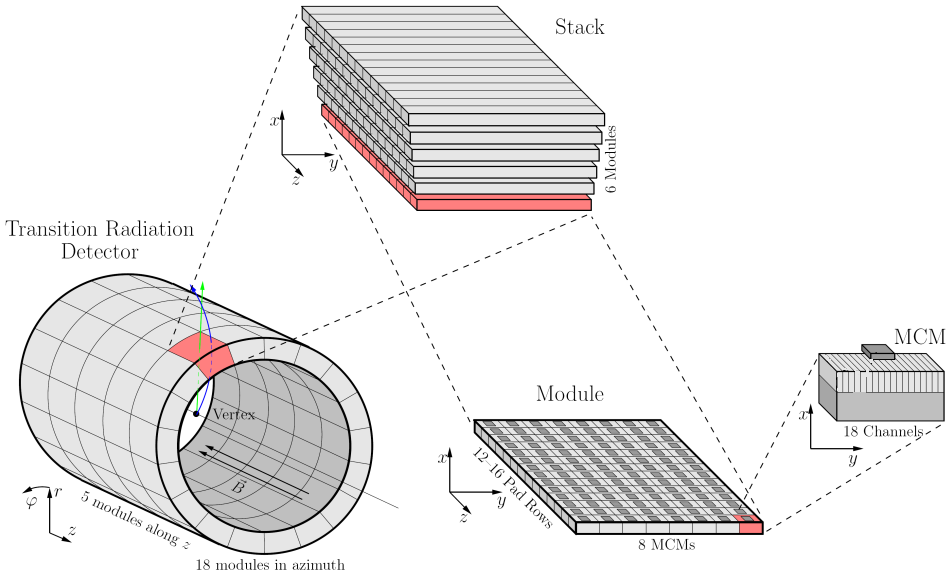

Figure 4.1: The layout and coordinate systems of the ALICE TRD [Cuv03].

4.1.1 Transition Radiation in the ALICE TRD

When a charged particle crosses the boundary of two media with different dielectric constants, it can emit part of its energy as transition radiation (TR). The average energy loss is approximately proportional to the relativistic Lorentz-factor γ [ALI01]:

$$\gamma = \frac{E}{m_0 \cdot c^2} = \frac{1}{\sqrt{1 - \frac{v^2}{c^2}}} \,. \tag{4.1}$$

For ultra-relativistic particles with $\gamma > 1000$, the energy of the TR photons is of the order of keV. These photons can be detected in gaseous detectors, for example. Slow particles can only generate TR with much lower energy and yield. These photons are absorbed by the radiator materials and are not detected. TR is emitted

[19] Actually, the number of chambers will be smaller. Because screening of the chambers would handicap the PHOS, three stacks will be left out, so the TRD will finally consist of 522 chambers. Since the software used in this thesis, especially the calibration software, computes 540 chambers, this quantity will be referred to in the following.

under small angles, mostly in a cone of $1/\gamma$ with respect to the direction of the charged particle.
However, the probability to emit TR in a single boundary crossing is very low, therefore radiators in TR detectors are made of foils, fibers and foams, providing a large number of boundaries to crossing particles.
In order to discriminate electrons from pions, the ALICE TRD exploits their different masses. With $511\,\mathrm{keV/c^2}$ rest mass, electrons and positrons are much lighter than $\pi^{\pm}$ with a rest mass of $140\,\mathrm{MeV/c^2}$ [eaPDG09]. Therefore, in the same momentum range, $e^{\pm}$ are much faster than $\pi^{\pm}$. Particle momenta of interest in the ALICE experiment lay between 1 and $100\,\mathrm{GeV/c}$. In this range, only the γ-factors of $e^{\pm}$ are large enough to generate detectable TR photons.

4.2 Readout Chambers

The 540 detector modules are composed of three parts of different functionality: A radiator, a multi-wire proportional chamber and readout electronics.

The radiator is built in a sandwich structure with two rohacell foam sheets of 0.8 cm thickness and a mat of 3.2 cm polypropylene fibers in between. This provides mechanical stability and sufficient TR efficiency at a reasonable thickness [ALI01]. A relativistic particle crossing the radiator generates 1.45 X-ray photons on the average [ALI08].
A readout chamber (ROC) of 3.7 cm thickness is mounted on top of the the 4.8 cm thick radiator, filled with a detector gas. It is designed as a time projection chamber with a drift volume followed by an amplification region. The chambers will be operated in such a way that they work as time projection chambers with a multi-wire proportional chamber (MWPC) readout. The top of the radiator serves as entrance window and drift electrode to the readout chamber. The drift region is 3 cm thick and ends at the cathode wires, set to ground potential. Figure 4.3 sketches a readout chamber. A homogeneous drift field of $700\,\mathrm{V/cm}$ will be applied, leading to a drift voltage of $-2.1\,\mathrm{kV}$. Between the drift wires and the pad plane, a plane of anode wires is installed, typically with a voltage of $+1.5\,\mathrm{kV}$. Both drift and anode wires are oriented in y-direction. In figure 4.2, the internal geometry is given. Between drift and anode wires, the electric field is inhomogeneous, and electrons passing this region gain enough energy to ionize other gas molecules. An avalanche of electrons is generated, the number of electrons per avalanche is proportional to the applied anode voltage.

By this design of a chamber, drift time and signal amplitude can be adjusted independently. A higher drift voltage leads to a shorter signal length, a higher anode

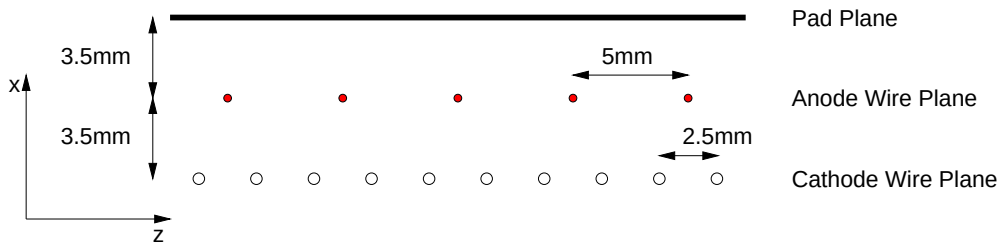

Figure 4.2: Wire geometry in TRD readout chambers [ALI01].

voltage leads to an increase of the signal amplitude.
The chambers are filled with $Xe/CO_2(85\%/15\%)$. Due to its large Z number, Xe has a high X-ray photoabsorption probability; CO_2 serves as quencher.
On top, facing the readout chamber, a pad plane is mounted. The plane is built of rhomboid shaped Cu-pads with an average length of 7.3 cm in z-direction and 0.9 cm in y-direction [ALI01]. With their average area of 6.3 cm^2, the pads are the smallest unit in the ALICE TRD and determine its granularity.

One layer of a TRD SM comprises 144 pad columns in y-direction and 76 pad rows in z-direction. Stack 2 chambers have 12 rows, all other chambers have 16, see figure 4.1. Like the drift wires, the pad plane is on ground potential. To improve position resolution in z, the pads are tilted by an angle $\varphi_t = \pm 2°$, opposite in consecutive layers.
The avalanche ionization at the anode wires induces a charge in the pads. The pads are connected to the readout electronics, that record the charge and generate a signal, see section 4.6. The processes involved in signal generation in the TRD are presented in the following section.

4.3 Signal Generation in TRD Readout Chambers

In the readout chambers (ROCs), a signal is generated in the following way: A fast, charged particle crosses the radiator which faces the beam axis. If its γ-factor is ≥ 1000, one or more TR photons will be generated in the radiator. In the ALICE experiment, this is only expected for electrons. Then, the charged particle crosses the readout chamber, where it ionizes the Xe-atoms. Since the primary particle is of relativistic velocity, it has immediately crossed the chamber and penetrates the next detector. In the drift region, electrons that have been liberated in the ionization process are exposed to the 700 V/cm drift field and travel towards the amplification region with constant velocity, see the top left panel in figure 4.3. In the amplification region, the strong field gradient in the vicinity of the anode wires

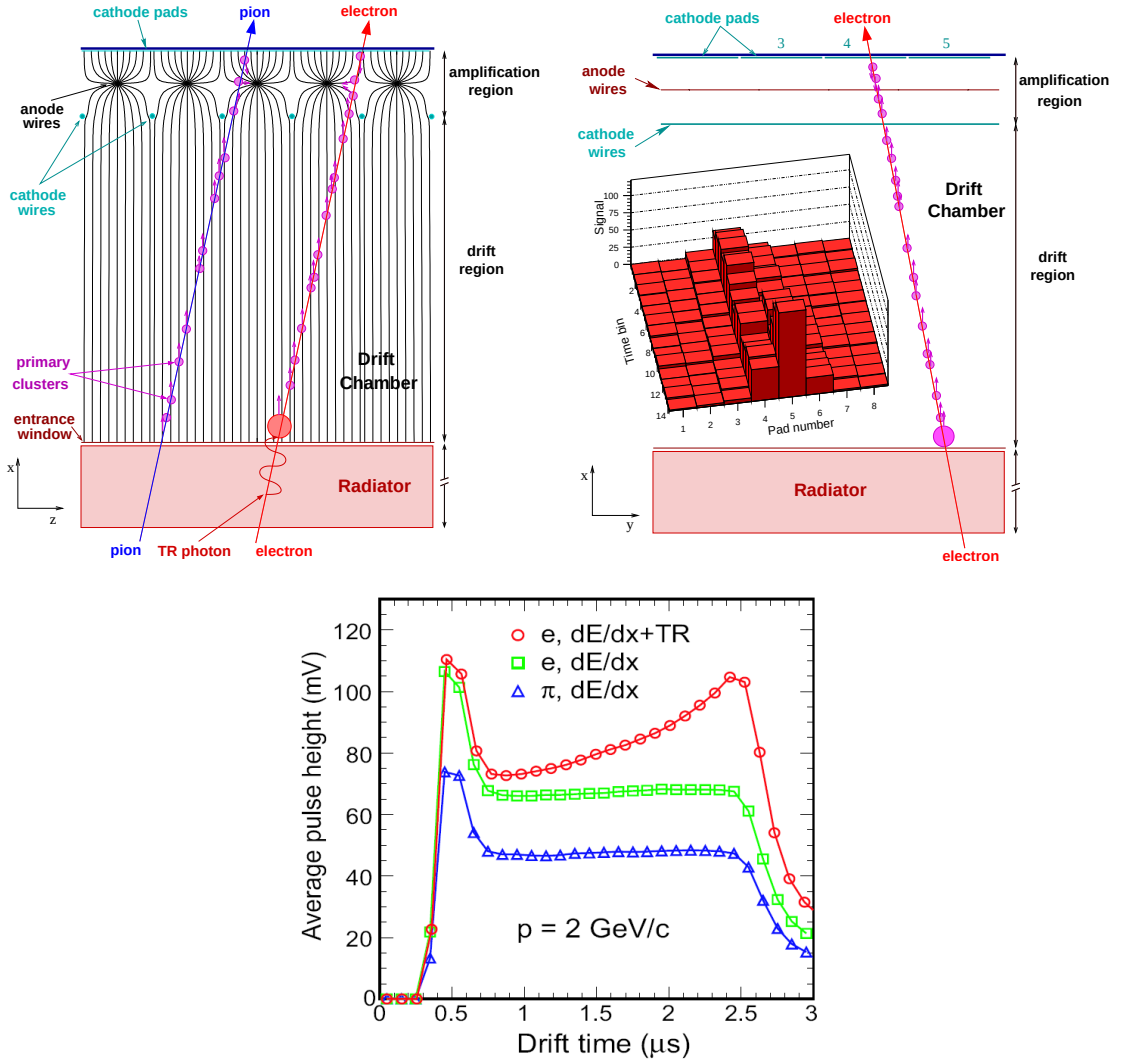

Figure 4.3: Top left panel: a TRD chamber in rz-direction crossed by an electron and a pion. Only the electron generates a TR photon in the radiator. Top right panel: resulting time signal for different pads and a chamber in $r\varphi$-direction [ALI01]. Bottom panel: average pulse heights as a function of the drift time for pions (triangles), electrons without TR (squares), and sum of electron and TR signal (circles) [ALI08].

leads to a large acceleration of the electrons which gain enough energy to ionize other gas atoms, so an avalanche of electrons is created. In less than a nanosecond, the electrons reach the anode wires and are dissipated. The ions move away from the anode wires towards the drift electrode with a velocity that is some thousand times smaller [ALI01]. This results in a positive space charge inducing a charge in the pad plane. Since the pad plane is subdivided into rows and columns, the y and

z-position of the track can be estimated, see top right panel in figure 4.3.

With 10 MHz sampling rate, on each pad the readout electronics record the signal as a discrete function of time. The bottom panel in figure 4.3 shows typical signals. The primary particle ionizes atoms above and underneath the anode wires. This charge is recorded first, represented by the amplification peak right at the beginning of the signals. Then, with a constant rate, electrons from the drift region reach the amplification region. For pions and electrons without TR, this results in a plateau. The Bethe-Bloch formula (equation 5.1) predicts that electrons lose more energy than pions on average in the given energy range, therefore the plateau is higher for electrons. If the electron has generated TR, the signal will rise at the end. The TR photons ionize gas atoms, too, which leads to an additional signal. Since these ionization processes take place mostly right behind the radiator, those additional electrons reach the amplification region last. The time signal provides the radial position of a track.
The particle identification, here the separation of electrons and pions, is done via the differences in charge deposit between their signals. The electron probability for each signal can be calculated with different methods. Likelihood [And04] as well as neural-network methods [Wil06] both exceed the design goal of factor 100 pion efficiency.

4.4 Gas Gain in TRD Readout Chambers

The gas amplification (gas gain) depends on a couple of variables, e.g. the type of detector gas, the atmospheric pressure, mechanical deformations of the chambers, or wire sag. Since most of these variables are fixed to a certain range in the TRD, the gain in this experiment will mostly be influenced by the anode voltage. In addition, the measured gas amplification of the detector is dependent on the incident angle of the track with respect to the pad plane.

Two points have to be taken into consideration. The bigger the incident angle perpendicular to the pad plane, the longer the distance the primary particle traverses in the chamber. And a longer distance results in a larger energy loss. Secondly, the positive ions in the amplification region attenuate the electric field and therefore attenuate the gain. As shown in figure 4.4 , this effect is less severe for larger angles. For angles $> 17°$ it can be neglected [ALI01]. Apart from the incident angle, the strength of the attenuation effect is dependent on the gain itself. As shown in figure 4.4, for higher gas gains the angle dependency would become too strong, so the design goal is a gain of 10^4, which appears to be a good compromise between gas amplification on one side and angle independence on the other side.

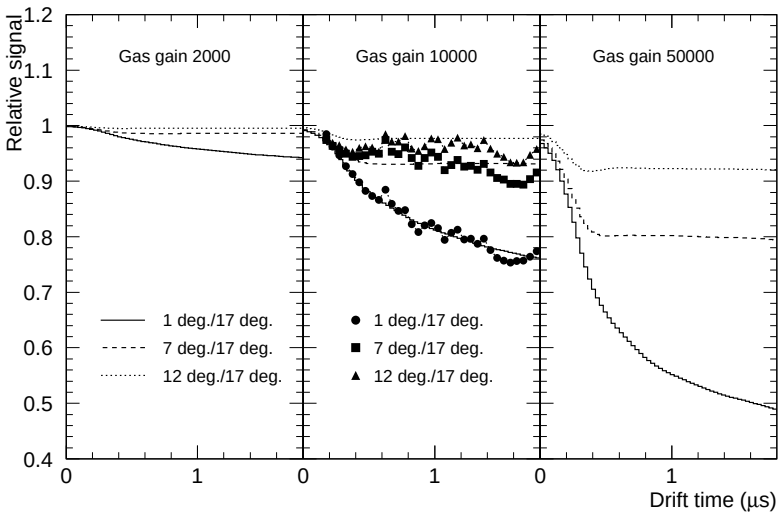

Figure 4.4: Calculated relative gain as a function of drift time for different angles and gain regimes. Data points are from prototype measurements [ALI01].

Both effects lead to a higher gain for particles under larger incident angles. Thus, for any gain measurement, exact knowledge of the track angle is crucial. Being the central part of this thesis, a general introduction to gas amplification in multiwire-proportional chambers will be given in chapter 5.

4.5 Pad and Time Response Function

The Pad Response Function (PRF) describes the fraction of the total charge induced on one single pad of the pad plane as a function of the track position. The induced charge in the pad plane is usually distributed over three pads. Since not only one pad contains information on the trajectory of the particle, the position resolution is improved when several pad signals are combined using the PRF. In good approximation, the charge is a Gaussian distribution for ALICE TRD chambers, see figure 4.5.

The Time Response Function (TRF) gives the overall time response of the detector to a given charge. For the TRD, two effects influence the shape of the signal.
The ions created in the avalanche have a rather slow drift velocity. It takes them several microseconds to disappear out of the amplification region. This results in an *ion tail* at the end of the signal. In addition, the response of the preamplifier/shaper (section 4.6) in the multi chip modules influences the shape of the signal. Figure 4.6 shows a simulation for the PRF. Obviously, the time response is not Gaussian.

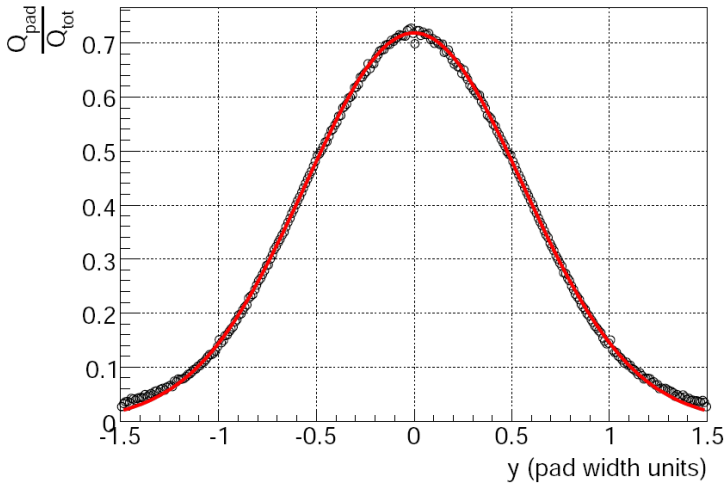

Figure 4.5: The pad response function of the TRD. Black dots represent means of the channels, the red line is a Gaussian fit to the PRF [Wul09].

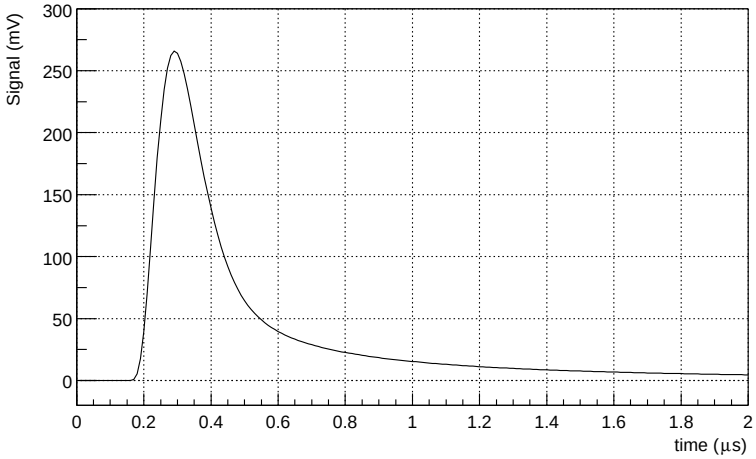

Figure 4.6: Simulated time response function of the TRD [ALI01].

4.6 Front-End Electronics

Along with working as a tracking detector, the TRD serves as a fast trigger for particles with high p_t as well. A trigger decision in the TRD has to be made in about 6 μs, therefore calculations have to be performed locally, directly in the electronics of the chambers. The chamber Front-End Electronics (FEE) digitize pad signals and calculate *tracklets*. A tracklet[20] is a linear fit of a particle track segment in

[20] In section 7.2 the different objects calculated during event reconstruction are described in more detail.

one ROC. In total, over one million channels are processed in the TRD FEE. As presented in figure 4.7, it can be subdivided into different logical components.

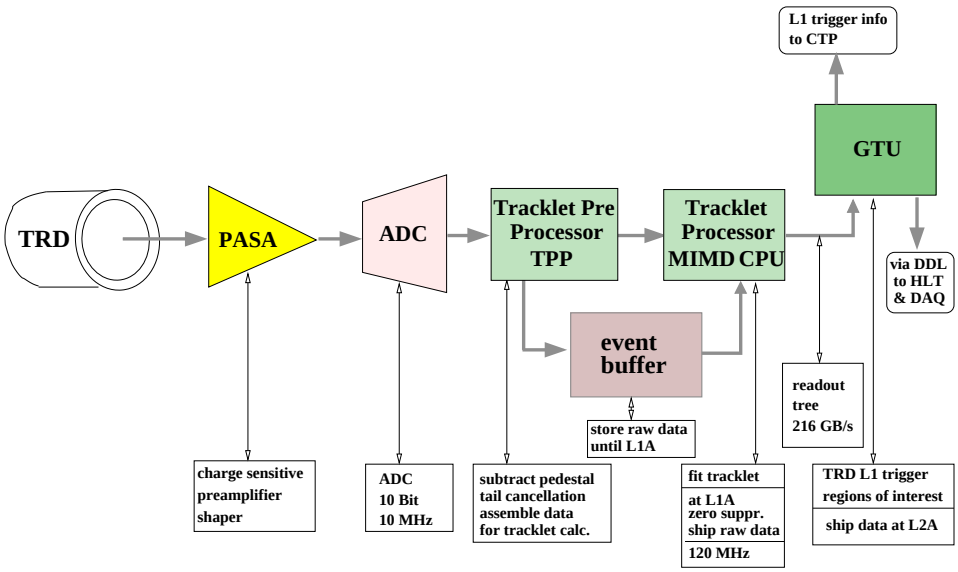

Figure 4.7: Logical components of the ALICE TRD Front-End Electronics [ALI08].

First, the pad signals are passing a charge sensitive PreAmplifier/ShAper (PASA) and then an Analog Digital Converter (ADC) with a 10 MHz sampling rate. In a data processing circuit, the data of subsequent time bins is stored in event buffers. During the drift time of the electrons, the Tracklet Pre-Processor (TPP) prepares information for the Tracklet Processor (TP). As part of the TPP, a digital filter is implemented. At the end of the drift time, the TP processes the data of all time bins and determines tracklets. The TP is a CPU implemented as a Multiple Instruction Multiple Data (MIMD) processor, operating at 120 MHz. The ADC, digital filter, TPP and TP are collectively called TRAcklet Processor (TRAP).

These units are mounted directly on the ROCs. The data are then shipped to the Global Tracking Unit (GTU) outside the chambers via optical fibers. The GTU combines the information of the individual TRD ROCs. It receives tracklets from all TRD readout chambers. If there are at least four matching tracklets in one stack, the GTU computes the particle track from the tracklets and sends a positive trigger signal to store the recorded data.

Except for the GTU, all these components are integrated in Multi-Chip-Modules (MCMs). Type C1 ROCs are equipped with 128 MCMs, C0 ROCs have 96 MCMs. A few additional MCMs are mounted on the ROCs, dedicated to merge the data.

In every ROC are eight MCMs in column direction, and every readout pad is connected to one of the 18 PASA channels of an MCM. Since charge in the pad plane is distributed on more than one pad (see section 4.5), to achieve good position resolution it is always necessary to combine signals of adjacent pads. Therefore, the MCMs have 21 ADC channels, where ADC channels 0,1 and 20 are connected with PASA outputs of neighbouring MCMs. If the MCM is located at a ROC border, interconnected channels without a corresponding pad are masked out. The connections are sketched in figure 9.17 of section 9.3.

The digital filter for the 21 ADC channels consists of five stages. The first stage is the nonlinearity correction. Here, nonlinear effects in the amplification and digitalization are remedied. The nonlinear transfer function is applied using a look-up table. The second stage is the pedestal correction. A recursive filter of first order cancels the individual channel pedestals and provides a global, well-defined baseline value of the signal that is usually 10 ADC counts. The next step is the gain correction.

Imperfections in the ROC geometry result in local fluctuations of the gas gain, imperfections in the fabrication of the electronics lead to differences in the amplification of the PASA and ADC channels. To correct for these three effects, gain calibration is implemented in the TRAP. Within one MCM, the gain correction looks as follows:

$$O_n(t) \;=\; \gamma_n \cdot I_n(t) \;+\; \varrho_n \;. \tag{4.2}$$

For the 21 ADC channels of an MCM, the output $O_n(t)$ of each channel n can be corrected to the same value within one MCM. Therefore, the input $I_n(t)$ is multiplied by a correction factor γ_n. With $0.875 \leq \gamma_n \leq 1.125 - 2^{-11}$, corrections are possible within a range of ± 12.5 %. Since gain correction is implemented behind the pedestal correction stage, the pedestal is shifted by γ_n as well. Therefore, a number ϱ_n has to be added in order to obtain the same pedestal in each channel. Variations in gain between PASAs of different MCMs can be corrected by adjusting the reference voltage of the ADC. It can be set to values between 1.05 V and 1.45 V, thus in a range of $\approx \pm 15$ %. This is not part of the digital filter.

The next step in the digital filter is the tail cancellation. The slow movement of the Xe-ions in the amplification region and the PASA response result in a long tail in the signals (see section 4.5). The tail can be treated as an exponential decay and is suppressed by a second order exponential progression. The last step is a crosstalk filter. The pads experience a capacitive coupling to their neighbours, i.e. a signal in one pad will always induce a signal in adjacent pads, this is called crosstalk. To suppress the crosstalk, a 2-dimensional filter matrix was implemented,

corresponding to the 2-dimensional pads. A detailed description of the FEE can be found in [L+05] and [Gut02].

5 Gain in Multi-Wire Proportional Chambers

5.1 Ionization Energy Loss

Charged particles crossing a gas lose energy due to ionization of the gas molecules. In the case of electrons, additional losses due to bremsstrahlung or TR have to be taken into account.
The average ionization energy loss per unit length is given by the Bethe-Bloch formula [Sau77]:

$$\left\langle \frac{dE}{dX} \right\rangle = -\frac{2\pi N_e e^4}{m_e c^2} \frac{z^2}{\beta^2} \left\{ \ln\left(\frac{2m_e c^2 \beta^2 \gamma^2 E_M}{I^2} - 2\beta^2 \right) \right\} , \tag{5.1}$$

where $m_e c^2$ represents the rest energy of an electron. The ionization potential I, and the number density of electrons in the medium $N_e = N_A \cdot Z/A \cdot \varrho$ are determined by the properties of the gas. The parameters depending on the charged particle are its charge z, its velocity β and its γ-factor. E_M represents the maximum energy transfer allowed in each interaction.
The ionization energy loss of a charged particle does only depend on its velocity β. At low velocities, $\left\langle \frac{dE}{dX} \right\rangle$ decreases proportionally to the $1/\beta^2$-factor in equation 5.1. For higher β, the electromagnetic field of the particle becomes relativistic and expands as $1/\gamma$ in the transverse direction. Therefore, the energy loss slightly increases again, this is called relativistic rise. At even higher β, the energy loss saturates around the same value for every sort of charged particle. One task of the ALICE TRD is to distinguish electrons from pions at high p_t. For momenta roughly above 10 GeV/c, $\pi^{\pm}$, $\mu^{\pm}$, and $e^{\pm}$ are already in the saturated part [Sau77], thus ionization energy loss cannot be used for this purpose in the TRD.

5.2 Amplification of the Signal - Gas Gain

In the TRD, about 850 electron-ion pairs are created by a minimum ionizing particle (MIP)[21] in the 3 cm range of the drift region. With a pad capacity of 20 pF, the signal would only have an amplitude of 2.36 μV [Bai09a]. As a consequence, amplification of the signal is absolutely necessary, that is why the TRD modules are operated as MWPCs as described in chapter 4.

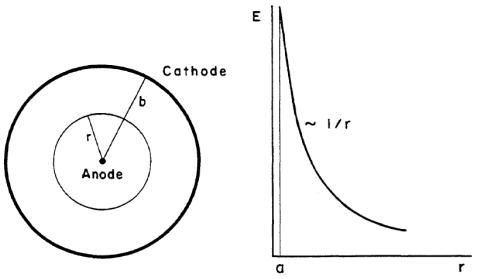

Figure 5.1: A coaxial cylindrical proportional counter and the shape of the electric field around the thin anode wire [Sau77].

A TRD readout chamber can be considered as an array of independent proportional counters. The electrical field in the vicinity of each anode wire is given by [BR94]:

$$E = \frac{\lambda}{2\pi\varepsilon_0}\,\frac{1}{r}\,, \tag{5.2}$$

where λ is the linear charge density and r is the wire radius. Figure 5.1 sketches an anode wire and the shape of the electrical field. One can easily see that it is necessary to use thin wires in order to obtain strong electrical field gradients. In TRD chambers, the anode wires have a radius of 10 μm [ALI01].
If the field is sufficiently high, the electrons gain enough energy to ionize other gas atoms. Thus an avalanche of electrons is created in the vicinity of each anode wire.

Usually noble gases are used as working gas for a detector, because this way avalanche creation can be achieved at lower E-fields than with complex molecules. This is due to the fact that complex molecules, e.g. CO_2 or CH_4, have additional rotation and vibration modes, hence provide more degrees of freedom to absorb the energy of the electrons before they reach the ionization energy. In TRD chambers,

[21] A particle at a momentum experiencing the lowest possible energy loss, given by the Bethe-Bloch formula.

xenon atoms are used, because they have a good absorption probability for TR in addition. Nevertheless, a MWPC cannot be operated when it is filled with a pure noble gas. During the avalanche process, the atoms are both ionized and excited. Excited noble gases can only return to their ground state by photon emission. These photons can eject electrons out of the metal electrodes by the photoelectric effect. The photoelectrons would start a second avalanche soon after the primary one. Therefore, a quenching gas with a complex molecular structure is added. Due to their additional, radiationless degrees of freedom, the molecules can absorb photons in a wide energy range. The TRD chambers are filled with a mixture of 85 % xenon and 15 % CO_2.

The ratio of the number of electrons in the avalanche and the number of drift electrons is called amplification factor or gas gain g. When the chamber is operated in proportional mode, the gain can be derived from the first Townsend coefficient α. The inverse of α corresponds to the mean free path between ionization processes, therefore α gives the number of ionizing particles produced per unit length per electron. Let N_e be the number of electrons at a given position. The increase of the number after a path dr is [Sau77]:

$$dN_e \;=\; N_e \alpha \; dr \; . \tag{5.3}$$

Integrating equation 5.3 from the starting point of the avalanche at r_0 to the surface of an anode wire with the radius r_a gives the amplification factor g [Sau77]:

$$g \;=\; \frac{N_e(r_a)}{N_e(r_0)} \;=\; \exp[\int_{r_0}^{r_a} \alpha(r) \; dr] \; . \tag{5.4}$$

It can be shown that for moderate gas gains, the amplification factor depends exponentially on the anode voltage [Sau77]. In the TRD, a rise of 3.6 % in the anode voltage from 1400 V to 1450 V would lead to a rise of the amplification factor of 72 % [ALI01]. Therefore, in order to avoid time variations of the gain, it is crucial to keep the anode voltage at a constant level.
Apart from the anode voltage, there are several effects that can influence the gain of an MWPC. The gas gain varies with the density ϱ of the gas, which is linearly dependent on the pressure and the temperature. For a relative increase in density of 1 %, the gain will decrease by about $\Delta g/g \sim (5-8)\%$ in common gas detectors [BR94]. As outlined in section 4.4, the gain depends on the incident angle of the track due to attenuation by the positive ions. In order to reduce this effect, the TRD will be operated at a moderate gain of 10^4 together with a relatively high anode voltage. In addition to these global effects, local variations of the gain, caused by mechanical imperfections of the chambers, occur as well:

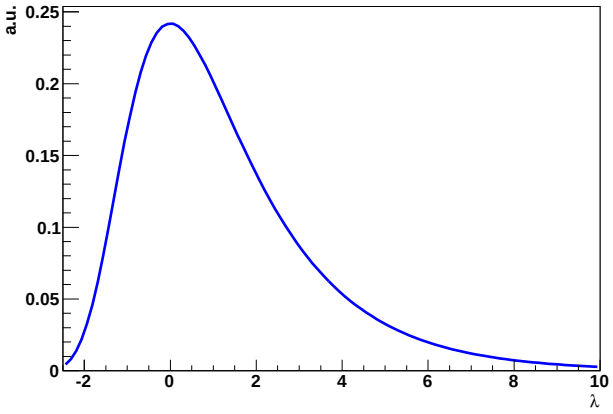

Figure 5.2: The normalized Landau distribution.

Only a finite amount of tension can be applied to the thin wires, therefore gravitational and electrostatic forces cause sagging of the wires. A gain variation below 3 % due to wire sag is expected for the TRD [ALI01]. The supporting frames and structures, especially at the chamber borders, have influence on the gain. Furthermore, mechanical forces or a pressure difference between the gas volume in the chamber and the atmosphere can cause deformations of the chamber, which lead to local gain variations, too.

5.3 Fluctuations of the Energy Loss

The Bethe-Bloch formula (5.1) for charged particles does only give the average energy loss per unit length. In thin gas layers, the total energy loss is accomplished by just a small amount of interactions. Each interaction has a wide range of possible energy transfers, therefore the energy loss is statistically distributed. In thin media, the energy loss of a charged particle follows a Landau distribution [Sau77], [BR94]:

$$f(\lambda) \;=\; \frac{1}{\sqrt{2\pi}}\, e^{-\frac{1}{2}(\lambda + e^{-\lambda})} \;. \tag{5.5}$$

The variable λ represents the normalized deviation from the most probable energy loss $(\Delta E)_{m.p.}$:

$$\lambda \;=\; \frac{\Delta E - (\Delta E)_{m.p.}}{\langle E \rangle} \;, \tag{5.6}$$

where ΔE is the actual energy loss for a given particle, and $\langle E \rangle$ is the average energy loss for a given path in a gas volume.

As shown in figure 5.2 , the Landau distribution is asymmetric: the distribution has a long tail towards higher energy losses, so the mean value is not equal to the most probable value (MPV). The cause of the tail are highly energetic, so-called δ-electrons. When the energy of an electron ejected in an ionization process is higher than the ionization potential of the detector gas, this δ-electron can ionize gas atoms, too, and produce additional drift electrons.
As a consequence of the large fluctuations in energy loss, any measurement on dE/dX has to accumulate a large number of tracks in order to obtain reliable results.

6 Experiments with Cosmic Rays in Münster

In absence of an accelerator, TRD supermodules can be tested and calibrated using cosmic rays. Cosmic radiation provides a good source for high energy particles.

6.1 Cosmic Radiation

6.1.1 Origin of Cosmic Radiation on the Earth

The interstellar space is crossed by a large amount of particles, the so-called primary cosmic radiation. On top of the atmosphere, the cosmic radiation is composed of about 79 % protons and 15 % α-particles [eaPDG09], although the exact composition is dependent on the energy of the particles. The energy spectrum is described by a power law [Y+06]:

$$I_N(E) \;=\; \text{const} \cdot E^{-\gamma} \;, \tag{6.1}$$

with $I_N(E)$ being the intensity[22] and E the energy. For particle energies $1\,\text{GeV} \leq E \leq 100\,\text{TeV}$, the intensity is proportional to $E^{-2.7}$. Particles at lower energy are decelerated by the solar wind as well as by the earth magnetic field, and might even be fully screened [Y+06]. The origin of primary cosmic radiation is not fully understood, but shockwaves from supernovae explosions, black hole radiation or pulsars as astronomic "accelerators" are believed to be the major source of the primary cosmic particles. In addition, solar flares contribute particles to the cosmic radiation.
In the atmosphere, mostly at an altitude of 15 - 20 km, the protons of the primary cosmic radiation interact with nitrogen and oxygen atoms in the air. As a result, secondary particles are generated. The secondary particles in the atmosphere consist mainly of pions and kaons, with a relation of 10 : 1. Due to their short half-lives most of these particles do not reach the ground. Figure 6.1 sketches three different mechanisms of creation of secondary particle cascades:

[22] In terms of $\frac{\text{nucleon}}{\text{cm}^2\,\text{sr}\,\text{GeV}}$.

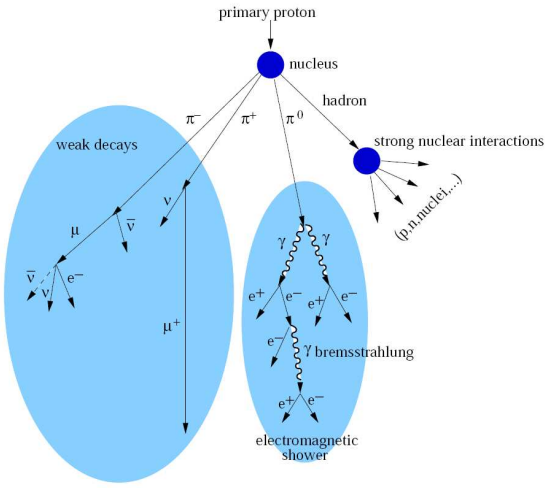

Figure 6.1: Interactions of a primary cosmic ray particle with atoms of the atmosphere. Different kinds of particle showers are generated [Hop04].

In *hadronic showers*, the secondary particles interact with the atmosphere in the same way as the primary particle. As a result, a shower of hadrons is generated. Its core consists mainly of pions.
The neutral pion decays into a pair of photons: $\pi^0 \longrightarrow \gamma + \gamma$. The photons produce electron-positron pairs. The result is an *electromagnetic shower*.
With a rate of 99 % [eaPDG09], the charged pions decay into muons and neutrinos due to *weak interaction*:

$$\pi^+ \longrightarrow \mu^+ + \nu_\mu \tag{6.2}$$
$$\pi^- \longrightarrow \mu^- + \bar{\nu}_\mu \, . \tag{6.3}$$

6.1.2 Cosmic Rays at Sea Level

With 80 %, muons are the main part of cosmic radiation at sea level. Muons decay into electrons and neutrinos:

$$\mu^+ \longrightarrow e^+ + \bar{\nu}_\mu + \nu_e \tag{6.4}$$
$$\mu^- \longrightarrow e^- + \nu_\mu + \bar{\nu}_e \, , \tag{6.5}$$

with a half-life of $\tau = 2.197 \cdot 10^{-6}\,\mathrm{s}$ [eaPDG09]. Most muons are generated at $\sim 15\,\mathrm{km}$ altitude in the atmosphere, on their way down to the surface they lose 2 GeV energy on average due to ionization processes. The mean energy of muons

at sea level is 4 GeV[Y+06]. As a consequence of the relativistic time dilatation, muons can cover the distance of about 15 km and reach the ground despite their short half-life. A 4 GeV muon has got a γ-factor of $\gamma = \frac{E}{m_\mu c^2} \approx 38$. This corresponds to a velocity of 0.99965 times the speed of light c, when the atmospheric energy loss is not taken into account. Due to the relativistic time dilatation $t = \gamma \cdot \tau$, the muon can travel about 25 km before decaying.
The intensity of muons at sea level is about $I \approx 1\,\mathrm{cm}^{-2}\mathrm{min}^{-1}$ [Y+06]. The uppermost chambers of a TRD supermodule (layer 5) cover an area of about 7.9 m^2, so around 1300 muons hit the layer 5 per second. The angular distribution of cosmic rays is propotional to $\cos^2\vartheta$, [23][Y+06] for muons energies ~ 3 GeV. At larger angles, the average muon energy increases because the particles have to cross a larger distance through the atmosphere. Lower energy muons decay before reaching the ground.

6.2 Experimental Setup in Münster

Measurements in this thesis were done with standalone supermodules (SM) in Münster. Here, cosmic rays (mostly $\mu^\pm$) serve as particle source. Since $\mu^\pm$ and $\pi^\pm$ have comparable masses[24], recorded signals in Münster correspond to $\pi^\pm$ signals in ALICE.
As substitute for the ALICE trigger system, in Münster the TRD SMs receive a trigger signal by a "cosmic trigger", placed above and underneath the SM as sketched in figures 6.2 and 6.3. Its purpose is to detect cosmic ray particles. Both parts of the cosmic trigger consist of organic scintillators linked to photomultipliers. Since the upper trigger is much shorter than an SM, it can be moved alongside its z-axis. The upper and lower planes are connected to a logical unit. It is possible to run the cosmic trigger in two operational modes: in coincidence mode or with the bottom trigger only.
In case of coincidence mode, a positive trigger signal is created if both detector planes detect a particle within a short time window. The dimensions of the cosmic trigger are chosen in such a way that a particle has to cross all six TRD layers to generate a coincidence signal. Given a positive trigger signal, all channels of the SM, i.e. the data of every single pad, are read out for this event. Due to their high velocities and the weak earth magnetic field, the trajectories of cosmic rays are almost straight. Thus, deducible from figures 6.2 and 6.3, the acceptance of the trigger is limited in φ- and z-direction. The maximum φ angle is $\sim 26°$. Based on these considerations, it is very unlikely to detect tracks at the chamber edges.

[23] The zenith angle ϑ gives the inclination of the particle with respect to the perpendicular.
[24] See table 2.1.

Nevertheless, there is a certain chance to hit the edges when several particles cross the detector at the same time, e.g. when a shower of particles is created by a primary cosmic particle. In coincidence mode, 94 % of all events contain one single track, 4.7 % are two track events [Sic09]. Typically, the trigger rate in coincidence mode is 80 Hz.
In a second mode, only the bottom trigger is used. If a particle crosses the bottom trigger, a so-called pretrigger is sent to the SM which then ships the tracklets to the Global Tracking Unit (GTU). The GTU decides whether to store the event. If at least four tracklets are found in one stack, the event is stored. The bottom trigger covers the whole SM in z-direction, the acceptance in φ is $\sim 58°$. Due to its size and larger acceptance, typically the bottom trigger rate is 300 Hz.

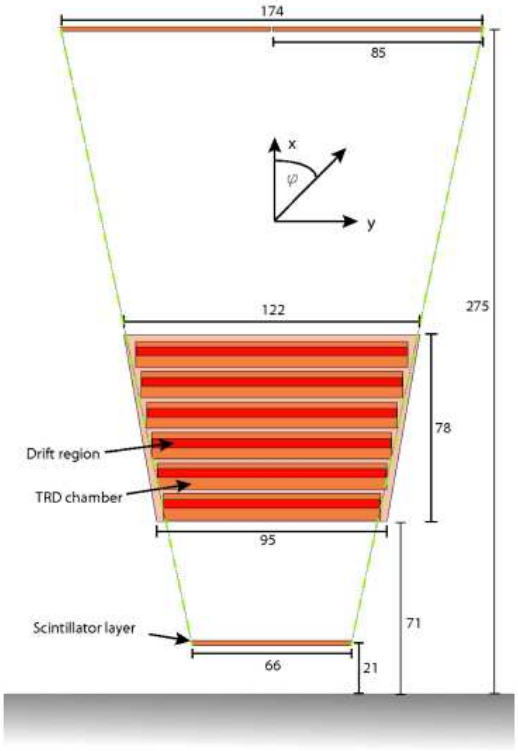

Figure 6.2: Front view of the cosmic trigger system with a TRD supermodule in between. Dimensions are given in centimeters [Bat07].

It turns out that that recorded tracks are not evenly distributed within the chambers. First, the angular distribution of cosmic tracks is a convolution of the acceptance of the trigger in φ and θ angle, and the angular distribution of cosmic rays at sea level $\propto \cos^2 \vartheta$. Second, the closer to the chamber edges, the more are trajectories limited to certain angles since a particle has to cross one or both trigger

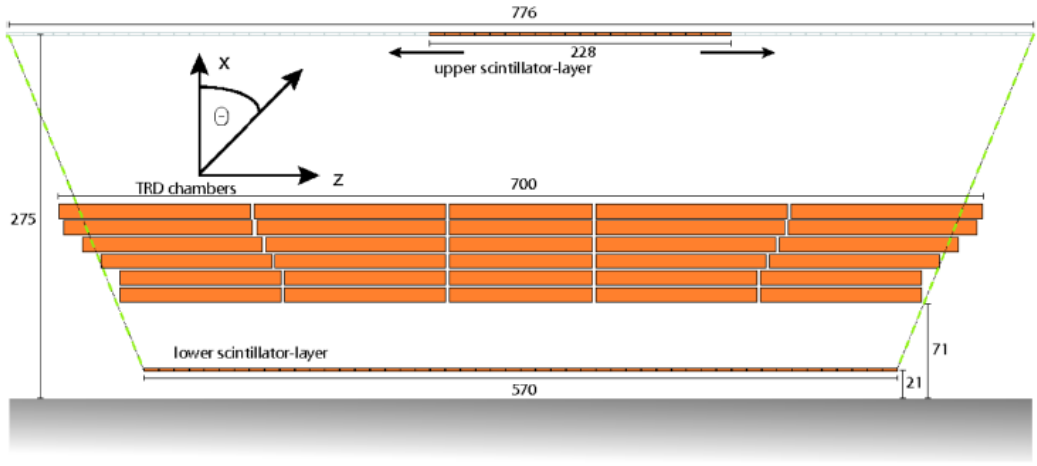

Figure 6.3: Side view of the cosmic trigger system with a TRD supermodule in between. Dimensions are given in centimeters [Bat07].

planes, respectively, too in order to be stored as an event. In addition, since at least four tracklets in the same stack have to be found in case of GTU decision, particles crossing the intermediate frames almost never generate a signal. As a consequence, most events contain tracks in the middle of the chamber, and the very edges are almost empty, as can be seen in figure 6.4. A calibration run in bottom trigger mode with a granularity of $(4, 5)$ is shown for the six layers of SM-I. Obviously, the number of recorded tracklets decreases towards the chamber edges. The low statistics in layer 4, stack 4 (row 59-75) can be explained by a lower anode voltage in this chamber. The lower statistics in layer 5 is due to problems in the tracking software. The horizontal lines of lower statistics match with border pads of different MCMs. The reason why smaller numbers of entries are found at the MCM borders is still unknown.

The gas system in Münster differs from the TRD gas system in ALICE, too. For economic reasons, $Ar/CO_2(83\%/17\%)$ instead of Xe/CO_2 is used as detector filling gas in Münster. Next to Xe/CO_2, Ar/CO_2 provides the best properties for particle detection with the ALICE TRD [ALI01].
In Münster, pairs of subsequent layers are connected each to one gas line, called "mix line". The three mix lines for an SM are connected to one gas input, for which the composition of the filling gas can be chosen. This provides the same filling gas in all mix lines. On the other hand, the flow and thus the pressure inside the chambers, can be adjusted individually for each mix line. Properties like gas composition and differential pressure can be monitored by an optical sensor for one mix line at a time.
Apart from that, a "flush line" is available. It provides a standalone gas input,

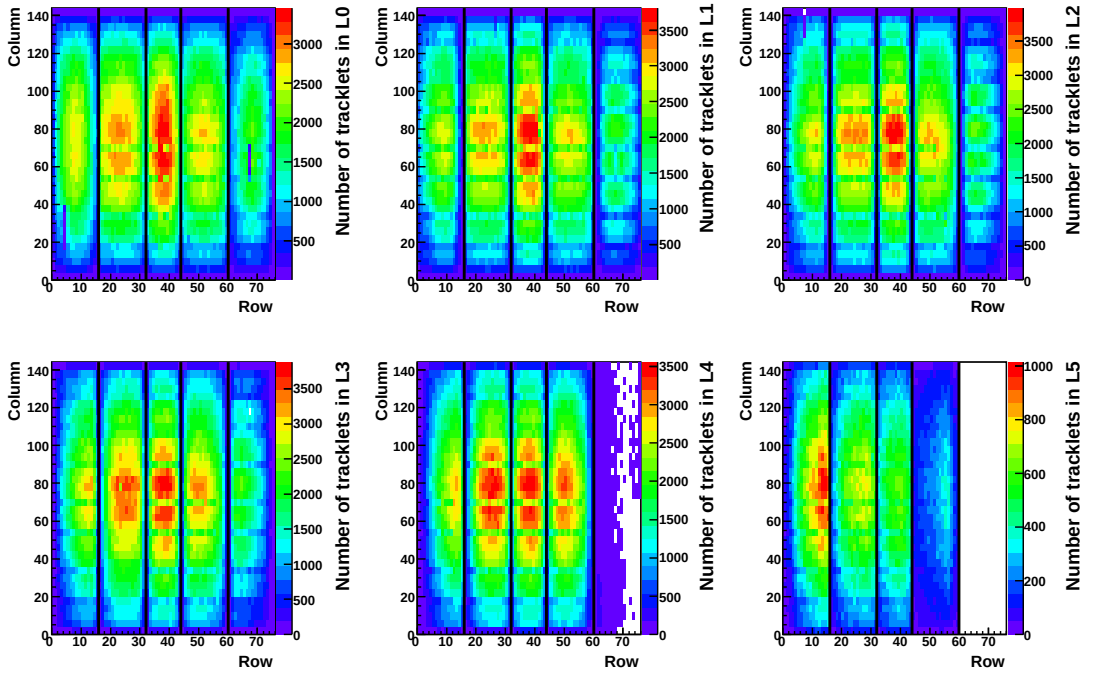

Figure 6.4: Number of tracklets per calibration group (each containing 4 pads in this plot) for 9 million events of run 2003 with the SM-I, shown for all 6 layers. The cosmic trigger was set to bottom trigger mode.

which is useful during the assembly of a SM. A detailed description of the gas system in Münster can be found in [Gri09].

6.2.1 Gain Calibration with Cosmic Rays

Given the experimental setup described above, the time it takes to accumulate enough statistics for a pad-wise gain calibration of a SM in Münster can be estimated.

For a first calculation we assume that hits from cosmic ray particles are evenly distributed across the SM. Each event should contain 4 tracklets in subsequent layers, and tracking problems in layer 5 are not taken into account. Furthermore, for a given event we assume that just one pad is read out for gain calibration, adjacent pads with smaller amplitudes are neglected. In order to obtain reliable gain factors, at least 1000 tracklets should have been found for each pad (see chapter 7).

With 144 pad columns, 76 pad rows, 6 layers and 4 tracklets per event, for a pad-wise gain calibration $1000 \cdot 144 \cdot 76 \cdot 6 : 4 \approx 16.5 \cdot 10^6$ events have to be recorded. Given the 300 Hz recording rate in bottom trigger mode, the measurement would take about 55,000 seconds or 15 hours.
In a more realistic estimation the time it takes for such a measurement is much longer. Since cosmic ray hits are very inhomogeneously distributed within a chamber, more events have to be recorded in order to accumulate sufficient statistics near the chamber borders. In addition, often the software used for event reconstruction did not compute a track for a recorded event, in fact nearly every second event appeared to be empty in the offline reconstruction. In figure 6.4, 9 million events were reconstructed and signals from each four neighbouring pads had to be integrated in order to accumulate enough entries.
From the experience gained with cosmic ray measurements on SMs, a pad-wise gain calibration would take 3 to 4 times longer than calculated above. That is at least 45 hours, recording 50 million events. Nevertheless, even in such a long term measurement not enough statistics would be accumulated for pads located directly at the chamber edges.

7 Calibration Procedure

The particle identification (PID) in the TRD readout chambers (ROCs) is based on the energy loss of the particles crossing the chambers. The energy loss is derived from the amplitude and shape of the pad signals, where the pad signal is to a large extend dependent on the gain. Therefore, in order to guarantee that a given particle leaves the same trace at any position in the TRD, a gain calibration for every pad is essential. In this chapter, the gain calibration procedure as it has been applied in this thesis will be explained. Although the measurements in this thesis were taken with standalone supermodules in Münster, the calibration procedure for the whole TRD at CERN will be the same.

7.1 Architecture of the Calibration Software

The calibration methods are implemented in the AliRoot framework [ALI09a]. This framework, written in the C++ language, is based on the ROOT data analysis software [Roo09]. It contains additional classes providing special functions for the ALICE experiment, e.g. detector simulation, event reconstruction, or gain calibration. The code development for gain calibration was subject to a PhD thesis in the year 2009 [Bai09a]. Together with the AliRoot classes, several macros outside AliRoot are provided to use these classes for calibration. In addition to calibration of the gain g, these classes allow for calibration of the average drift velocity v_d, the time offset t_0 of the signal, and the width σ_{PRF} of the PRF. The calibration macros use reconstructed tracks stored in a data format named ESD. The next section will outline the standard data processing in the ALICE TRD.

7.2 Event Reconstruction in the ALICE TRD

As described in section 4.6 , the data from the TRD is shipped to the GTU, where a trigger decision can be made. The output of the GTU are so-called raw-files that are stored in the ROOT file format `*.root`.
A second reconstruction is done offline with a grid of CPUs later on. Here, the

data are converted into different objects according to the step of the analysis. An *event* is a positive trigger decision, e.g. when a particle has presumably crossed the detector. The digitized signals of the readout pads are named *digits*. An algorithm looks for regions of digits generated by the same particle during a given time bin, called *clusters*. A *tracklet* is then built from a linear fit of all clusters presumably belonging to the same particle in one ROC. The trajectory of a particle in the detector is called a *track*. Tracks are reconstructed from the tracklets from different layers of one stack. They contain the x-, y-, and z-position of the particle, as well as its angles in φ- and θ-direction. The output of the reconstruction is stored in so-called `Event Summary Data` (ESD). General track information is saved in `AliESDs.root`. The file `AliESDfriends.root` contains additional information on the events, e.g. energy desposits needed for gain calibration [Sic09]. The ESDs can be processed on an event-by-event basis.

7.3 Gain Calibration with AliRoot Software

The gain calibration is based on the energy loss distribution dE/dX of the charged particles in the detector. In pp and PbPb-collisions, mainly pions are created that do not produce TR in the TRD. In Münster, cosmic muons are used which do not generate TR, either.
Furthermore, it is a relative calibration, i.e. ideally a pad has a gain factor of $g = 1$. For each calibration run, the pad data can either be compared to an arbitrary, default database (DB) where all pads are set to a global gain factor of 1, or to a previously generated DB in order to monitor changes in gain. A relative calibration has the advantage that systematic errors and uncertainties are cancelled out.

The gain calibration can be performed at different granularities of the detector, where groups of adjacent pads are summarized in *calibration groups*. At the largest granularity, a mean gain factor is derived for every ROC, so in this case there will be 540 calibration groups in the TRD. At the finest granularity, one gain factor is derived for each pad of the $1,181,952$ pads in the TRD.
Two parameters are passed to the calibration macros as shown in table 7.1, where nz determines the granularity in column direction (negative z-direction) and $nrphi$ determines the granularity in row direction (negative y-direction). With $(nz, nrphi) = (0, 0)$, the calibration sofware is set to the largest granularity, a pad-by-pad calibration is performed with $(nz, nrphi) = (4, 6)$. Figure 7.1 sketches a calibration with $(nz, nrphi) = (2, 2)$ for a C1 chamber and illustrates the group numbering.

Mode $nrphi$(col)/nz(row)	1	2	3	4
1	$(2 \cdot 2)$	$(2 \cdot 4)$	$(2 \cdot (N_{Row}/2))$	$(2 \cdot N_{Row})$
2	$(4 \cdot 2)$	$(4 \cdot 4)$	$(4 \cdot (N_{Row}/2))$	$(4 \cdot N_{Row})$
3	$(8 \cdot 2)$	$(8 \cdot 4)$	$(8 \cdot (N_{Row}/2))$	$(8 \cdot N_{Row})$
4	$(16 \cdot 2)$	$(16 \cdot 4)$	$(16 \cdot (N_{Row}/2))$	$(16 \cdot N_{Row})$
5	$(36 \cdot 2)$	$(36 \cdot 4)$	$(36 \cdot (N_{Row}/2))$	$(36 \cdot N_{Row})$
6	$(144 \cdot 2)$	$(144 \cdot 4)$	$(144 \cdot (N_{Row}/2))$	$(144 \cdot N_{Row})$

Table 7.1: Subdivision of TRD readout chambers into *calibration groups*. According to the division of pad groups in row and column direction (mode), the number of calibration groups (groups in pad column)·(groups in pad row) is given. $N_{Row} = 12$ for C0 chambers (stack 2), $N_{Row} = 16$ for the others [Bai09a].

In this example, every ROC is subdivided into 16 calibration groups. Each group contains $4 \times 36 = 144$ pads.

The gain calibration is separated in two parts: First, the dE/dX spectra are filled for every calibration group. Then, for each group the relative gain factors are derived from the dE/dX spectrum.

7.3.1 Filling of the dE/dX Spectra

A macro named `AliAnalysisTaskTRDCalib.cxx` uses the AliRoot class `AliTRDCalibraFillHisto`. It processes the ESDs event by event and stores the dE/dX spectrum for every calibration group to a file named `TRDCalibration.root`. Before storing the data, several corrections are made:

- As outlined in section 4.4, the track angles influence the amount of energy deposited in the gas. In ALICE, this means that tracks with a large pseudorapidity, i.e. a flat polar angle Θ (stack 0 and 4), traverse a larger distance in the chambers and deposit more energy. A systematically higher gain would be reconstructed for these tracks. The tracks can be inclined in φ, too. For that reason, the angles of each track have to be determined and the energy deposit per unit length has to be corrected for it. In ALICE, the determination of the track angles can be improved, if TPC tracking data is also taken into account.
- Previous gain corrections have to be taken into consideration. In order to obtain the correct amplification factors, it is essential to know whether the

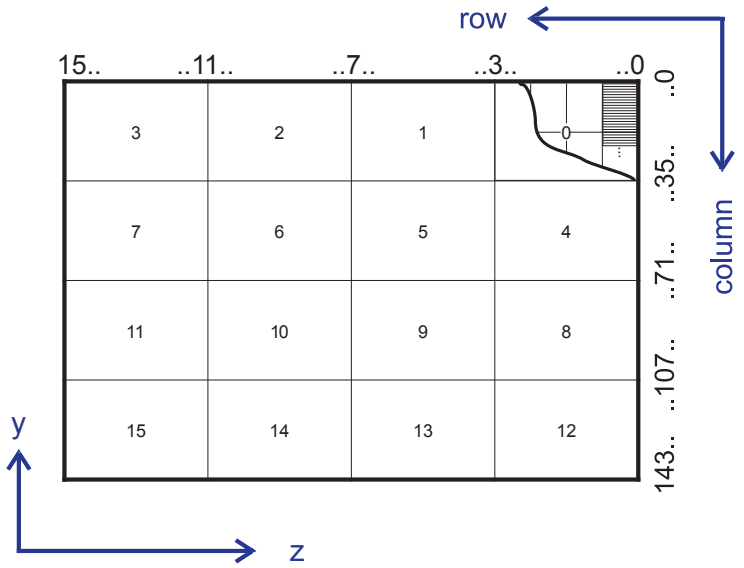

Figure 7.1: Division of a C1 readout chamber into calibration groups at a granularity of $(nz, nrphi) = (2, 2)$. In this case, 144 pads belong to each calibration group. The numbering of calibration groups, rows and columns is given. The detailed section in the top right corner sketches MCM and pad borders.

data have already been corrected with a previous DB. Therefore, it is possible to pass a DB to the calibration software. When calculating the new amplification factors, the former factors are taken into account.

- It is possible to compute the dE/dX distributions using only time bins that belong either to the drift or the amplification region of the signal. Nevertheless, for a first calibration, the whole range of time bins is stored [Bai09a].

Figure 7.2 shows a histogram filled with the spectra of a chamber-by-chamber calibration for the supermodule SM-II. Since data was taken with just one SM instead of the whole TRD, only the first 30 calibration groups are populated. The z-axis contains the number of entries, the y-axis gives the calibration group, and the x-axis contains the energy loss in arbitrary units. One can easily identify the Landau distributed shape of the energy loss.

7.3.2 Calculation of the Relative Amplification Factors

The `TRDCalibration.root` file is processed by a macro named `determineCoeff.C` which uses the AliRoot classes `AliTRDCalibraFit`, `AliTRDCalibraVector` and

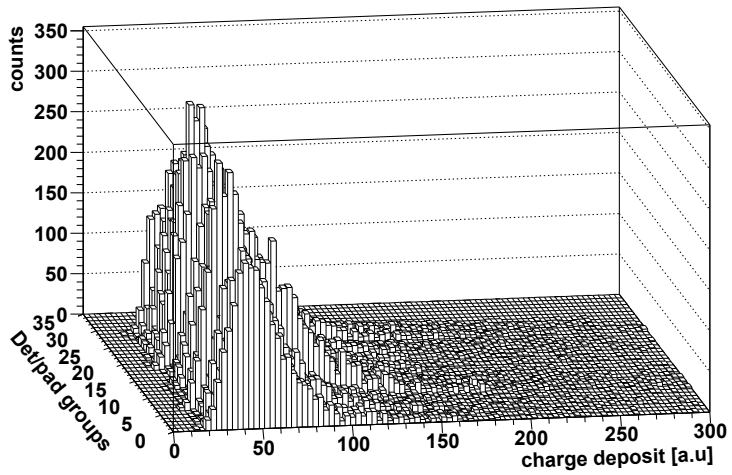

Figure 7.2: The dE/dX spectra of the 30 readout chambers (each a calibration group in this case) in SM-II, taken from the run 1899.

`AliTRDCalibraMode`. For the gain calibration, several algorithms are implemented that differ in accuracy, stability and the needed CPU time. The different methods were evaluated with simulated data and the *weighted mean* was chosen as the default method. It provides the best stability and the second best accuracy together with the shortest CPU time needed [Bai09a]. In this thesis, the weighted mean method was used for gain calibration, it is described in the following.

It is difficult to determine the mean of the energy loss distribution, because the mean is very sensitive to the long tail of the Landau distribution. Just a few particles with a huge energy loss can significantly shift the mean to higher gas gains. Therefore, the Most Probable Value (MPV) of the distribution is a better candidate to calibrate the gas gain relatively. The energy loss distribution can be fitted with the convolution of a Gaussian and a Landau function to determine the MPV. A more stable and CPU time efficient method is the weighted mean, where a weighting function $\omega(\Delta E)$ is introduced. The idea is that $\omega(\Delta E)$ should be the smaller the bigger the energy loss, so that the long tail only plays a marginal role. The measured dE/dX can be considered as a function $N(\Delta E)$, representing the number of tracks with an energy loss of ΔE in the calibration group. The weighted mean M_w is then defined as [Bai09a]:

$$M_w = \frac{\int_0^{\Delta E_{max}} \omega(\Delta E) \cdot N(\Delta E) \cdot \Delta E \, d\Delta E}{\int_0^{\Delta E_{max}} \omega(\Delta E) \cdot N(\Delta E) \, d\Delta E} = \frac{\sum_i \omega(\Delta E_i) \cdot N(\Delta E_i) \cdot \Delta E_i}{\sum_i \omega(\Delta E_i) \cdot N(\Delta E_i)} \,. \tag{7.1}$$

In order to calculate M_w, only the relative values of $\omega(\Delta E)$ need to be known. If $\omega(\Delta E) = \text{const} = 1$, M_w is simply the mean value of the energy loss.
The weighting function $\omega(\Delta E)$ has to be determined once with a typical dE/dX distribution. Therefore, $\omega(\Delta E)$ has been parameterized with a polynomial of 5 parameters (a, b, c, d, e) so that the weighted mean gives the MPV of the distribution [Bai09a]:

$$\omega(\Delta E) \;=\; a \;+\; b \cdot r(\Delta E) \;+\; c \cdot r^2(\Delta E) \;+\; d \cdot r^3(\Delta E) \;+\; e \cdot r^4(\Delta E)\,. \qquad (7.2)$$

With $0 \leq r(\Delta E) \leq 1$, the variable in the polynomial function is defined as [Bai09a]:

$$r(\Delta E) \;=\; \frac{\int_0^{\Delta E} N(\Delta e)\; d\Delta e}{\int_0^{\Delta E_{max}} N(\Delta e)\; d\Delta e} \;=\; \frac{\sum_{i=bin(0)}^{bin(\Delta E)} N(\Delta e_i)}{\sum_i N(\Delta e_i)}\,. \qquad (7.3)$$

The procedure is described in the following: An energy deposit ΔE is chosen. All counts from 0 to ΔE are summed and divided by the total number of counts. This is done for all energy deposits ΔE. Then $\omega(\Delta E)$ in equation 7.1 is substituted by equations 7.2 and 7.3. The parameters (a, b, c, d, e) are adjusted until M_w gives the same MPV as the convolution of Gaussian and Landau distribution fits.

The weighting function has been determined and is included in the AliRoot classes. In order to obtain a relative error for the calculated gain factors of $\sigma_{rel} < 2\%$, there should be at least 1000 reconstructed tracklets per calibration group for the weighted mean method [Bai09a]. The output of `determineCoeff.C` is written to a database (OCDB) containing the gain factors for each pad (eventually as a mean of its calibration group).

7.4 Offline Conditions Data Base

At the end of a successful gain calibration, two subdirectories are created: `TRD/Calib/LocalGainFactor/` and `TRD/Calib/ChamberGainFactor/`, where the amplification factors of each pad and the mean gain of each ROC are stored in ROOT files. The subdirectories are part of the Offline Conditions Data Base (OCDB) [ALI09a]. Along with TRD gain factors, the OCDB contains other calibration objects like the drift velocities, the starting points t_0 of the signals, or the alignment objects.
In ALICE, each OCDB will be stored to the ALICE Environment (AliEn) [ALI09b]. AliEn is a grid framework providing access to the hardware resources (Grid) as well as services like file catalogues, graphical user interfaces or job monitoring. It will be used for reconstruction and analysis of the ALICE data, a description of AliEn and

the Grid can be found for example in [Meo05]. In this thesis, we took advantage of the possibility to create a private OCDB on a local machine. The calibration software is able to take previous OCDBs into account and update the gain factors to a new OCDB.

If there are not enough statistics in a calibration group to perform a reliable calibration, the gain factor for this group is set to 1 by default. For the reconstruction of events (ESD production), the pad signals will be divided by the associated amplification factors in this database.

8 Tests of the Calibration Software

8.1 Accuracy Estimated with Cosmic Ray Data

In order to test the accuracy of the calibration procedure, a long time cosmic run taken with SM-I in bottom trigger mode was investigated.

Numerical simulations showed that the error of the weighted mean method depends on the number of analyzed tracklets in a given calibration group [Bai09a]. To confirm this results with cosmic ray data, the idea was to calibrate different datasets of the same size, and to determine the standard deviation of the computed gain factors for the given number of entries. If this is repeated for datasets with different numbers of entries, the standard deviation of the weighted mean method in dependence of the number of analyzed tracklets would be determined.
This method requires the gain to be constant during the time of data taking. As a first step of the analysis, parts of the SM with a large number of entries were selected. In the given run, most entries were found in the ROCs of stack 1. Due to problems with the tracking software, very few reconstructed tracklets are stored in the ESDs for layer 5, which makes it impossible to compute reliable gain factors for this layer. Therefore, layer 5 was completely left out of the analysis.

Then, 25 datasets were calibrated with two different granularities, on the one hand with a chamber-by-chamber resolution, and on the other hand with (3,2) granularity. In the second case, each ROC is subdivided into 32 calibration groups, and in each chamber the gain factors of group 20 (column 71-107, row 7-9) were investigated.

Unfortunately, in the investigated run the gain seems to increase with time. Figure 8.1 shows the behaviour of the ROC in layer 4, stack 1 at (0,0) granularity and figure 8.2 for group 20 at (3,2) granularity. This particular ROC is shown because the observed effect is strongest in this chamber, but every chamber shows an increasing gain. Since only the run number 2003 provides enough statistics for this analysis, no other run could be tested. The number of entries scales with the number of analyzed files. Each line in these plots represents five gain calibrations with a given number

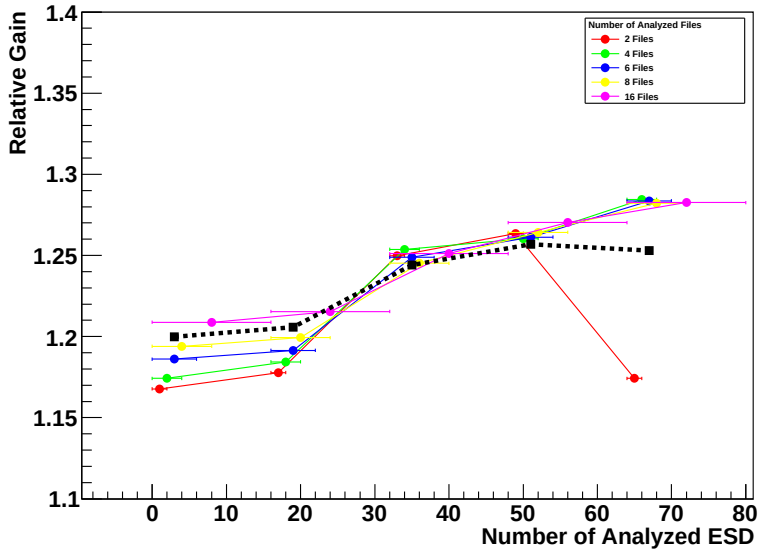

Figure 8.1: Computed gain factors for L4S1 in SM-I for the run 2003 at (0,0) granularity. The lines represent calibrations at different times with a given number of analyzed files. The dashed black line represents the mean gain of the SM.

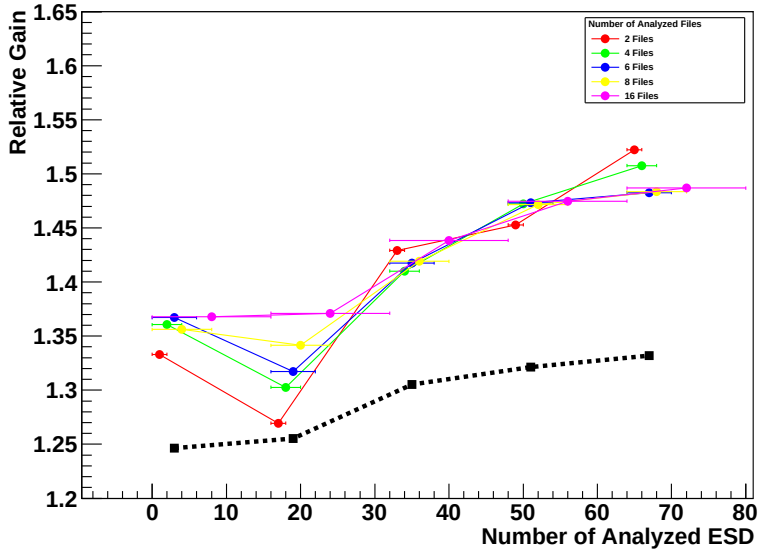

Figure 8.2: Computed gain factors for L4S1 in SM-I for the run 2003 at (3,2) granularity. The lines represent calibrations at different times with a given number of analyzed files for calibration group 20. The dashed black line represents the mean gain of the SM.

of analyzed files (ESDs) for different parts of the run, and therefore different time ranges. A new ESD is filled after 150,000 events are recorded. Given the 300 Hz of cosmic ray events in bottom trigger mode, each ESD represents a time range of about eight minutes. The bars in x-direction and the different colours indicate the number of analyzed files (2,4,6,8 or 16). The outlier for a two file analysis at 64 ESDs might be due to trigger problems in this time interval.

In both plots, the black squares connected by a dashed black line represent the mean of the gain factors for one calibration group, calculated for all five file sizes over the whole SM. In order to remedy global changes in gain, the calculated gain factors were divided by the SM mean. Residual changes should be caused by the error of the calibration software. On the other hand, they can also appear due to local parameter changes in the chambers.
In order to estimate the accuracy of the calibration procedure in dependence of the number of entries in a calibration group, the gain factors were normalized to the SM mean. Then the standard deviations σ of the normalized gain factors were calculated for each layer. Since a relative calibration is performed, the relative σ are given. The plots in figures 8.3 and 8.4 show the results. A data point represents the relative standard deviation of five gain factors computed for five different time intervals, for a given file size and layer in stack 1. The lines represent different layers. The error bars are given by the standard deviation of the number of entries in the calibration group in different time intervals.

Figure 8.3 shows the results for (3,2) granularity. In addition, a part of the results of the simulation is shown (see also figure 8.5), represented by a dashed line and blue squares. Only the results for layer 4 are comparable to the simulation. Looking at the data of the other layers, it seems that the error of the calibration is smaller than the error of the simulation for a given number of entries. The differences between the layers are not well understood, but at least the results of all layers are of the same order.
In figure 8.4, results for (0,0) granularity are shown. Since the calibration groups accumulate in this case far more readout pads, the number of entries is much larger than for (3,2) granularity. Simulated data is not available for these large numbers. Especially for layers 2 and 4, the curves do not follow up the curves for smaller numbers of entries which might be due to local gain variations in the chambers. This would have a larger effect on small parts of a chamber ((3,2) granularity) compared to the chamber mean ((0,0) granularity).

In summary, the relative standard deviations of the weighted mean method, estimated by cosmic ray measurements, lay roughly between 1 - 4 % for small numbers of entries, and seem to saturate at 0.5 - 1 % for more than 40,000 entries.

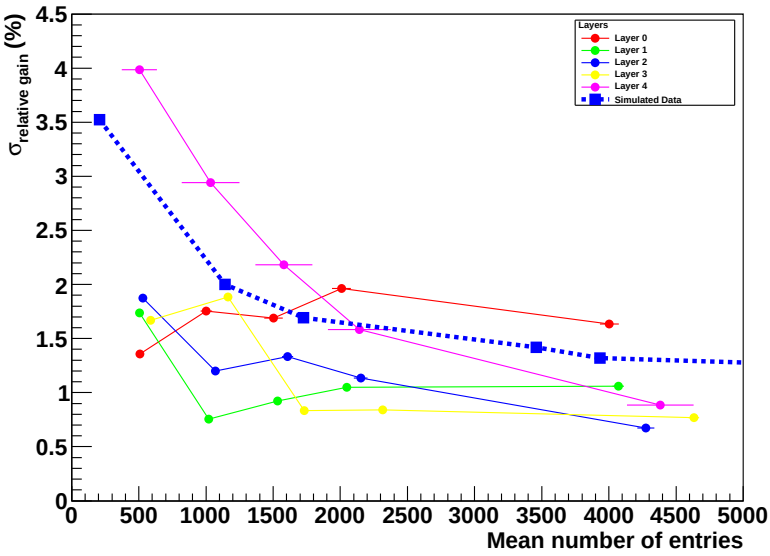

Figure 8.3: Relative standard deviation of computed gain factors at (3,2) granularity vs. the mean number of entries in the analyzed files for calibration groups in stack 1. The gain factors were divided by the mean gain of the whole SM before. Blue squares represent results of simulations [Bai09a].

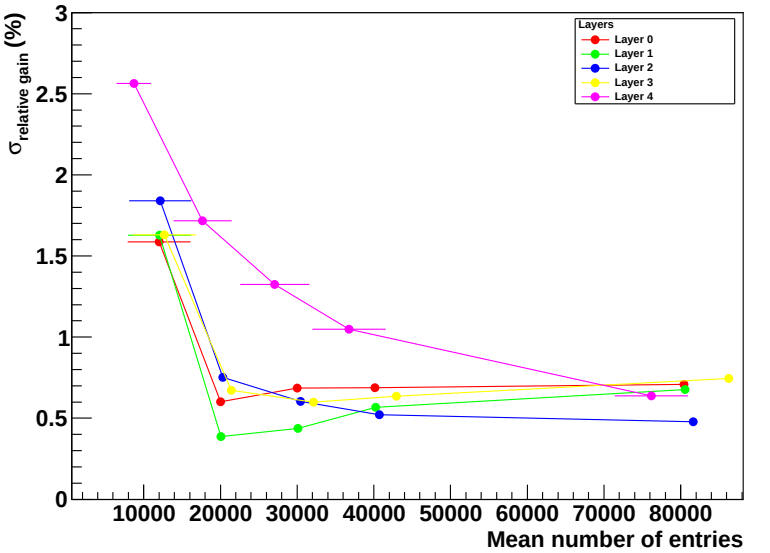

Figure 8.4: Relative standard deviation of computed gain factors at (0,0) granularity vs. the mean number of entries in the analyzed files for calibration groups in stack 1. The gain factors were divided by the mean gain of the whole SM before.

In the analyzed run, the gain seems to vary with time. On the whole, the analyzed files cover a time range of about 11 hours. Changes of the atmospheric pressure, for example, or changes of the temperature in the laboratory can easily occur on such time scales and influence the gain. Testing the accuracy of the calibration algorithm requires a perfectly stable gain. The normalization of the computed gain factors to the SM mean improved the results, but still, this seems not to remedy time variations completely. Despite these uncertainties, the calculated relative standard deviations are of the same order as those produced with simulated data. A simulation provides stable, well known gain factors and is a better test for the accuracy of the software. In addition, most analyses in this thesis are done with numbers of entries between 100 and 1000. When the calibration software itself is used to determine the error of the calibration, it is hard to obtain reliable data points for these small numbers of entries. Therefore, in the following section the simulation was taken into account for an error estimation.

8.2 Accuracy Estimated with Simulated Data

Figure 8.5 shows the accuracy for the weighted mean method represented by the blue squares, as derived from simulated data. Different fit functions were tested to describe the accuracy in dependence of the number of entries in a calibration group. For a large number of entries n, the measured dE/dX distributions are more accurate, allowing for a better determination of the gain factors. Thus the accuracy should scale with a function $f(1/n)$. In addition, since the error does not seem to vanish even for very large numbers of entries, a residual error was taken into account. According to the Gaussian law of error propagation, as a first fit function

$$\sigma = \sqrt{\left(\frac{p0}{\sqrt{n}}\right)^2 + (p1)^2} \tag{8.1}$$

was chosen, where n is the number of entries, $p0$ and $p1$ are constants. The result of the fit is represented by the red line in figure 8.5. Function 8.1 approximately describes the shape of the data, but it underestimates the errors for small numbers of entries. Then,

$$\sigma = \frac{p0}{\sqrt{n}} + p1 \tag{8.2}$$

was tested to fit the data. The result is represented by the black line in figure 8.5. This function describes the data in a better way. Obviously, the accuracy scales with $1/\sqrt{n}$. For very large numbers of entries, the error might saturate at the value $p1$ (compare also with figure 8.4). A residual error could be explained on

the one hand by errors of the calibration method itself. The weighted mean does not compute exactly the same results as a convolution of Gaussian and Landau distributions. On the other hand, for numbers of entries around 6000, all investigated methods seem to have a residual error around 1.5 % or higher. Thus, a better explanation could be that $p1$ describes all systematic errors of the dE/dX spectra, given for example by uncertainties in the tracking algorithm [Bai09b].
The fit function 8.2 becomes large for small numbers of entries, and even infinitely large for n = 0. Since the gain factors are derived from dE/dX spectra, a calibration does only make sense if enough statistics have been accumulated to fill a Landau shaped spectrum. Therefore, in this thesis, calibrations are only performed when there are at least 100 entries in a calibration group. If less entries are filled, no gain factors are derived and the gain is set to default 1. To avoid unrealistic error bars in these cases, the standard deviation is set to 0 if there are less than 100 entries in a calibration group.

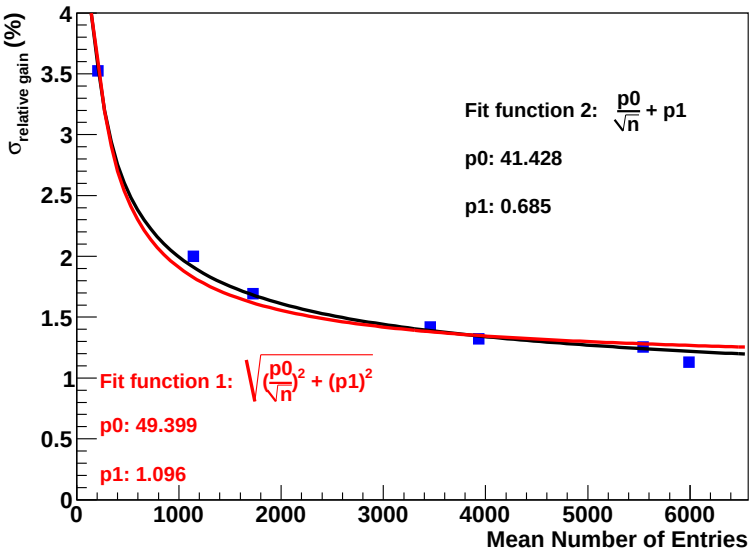

Figure 8.5: Relative accuracy of the weighted mean method vs. number of entries. Blue squares represent simulated data [Bai09a], the black and red lines are fits through the data points.

As a result, the relative error of the computed gain factors will be derived by the following empirical formula:

$$\sigma_{rel}(n) \;=\; \begin{cases} (\frac{41.428}{\sqrt{n}} + 0.685)\ \% & \text{for } n \geq 100 \\ 0\ \% & \text{else .} \end{cases} \tag{8.3}$$

8.3 Convergence

This section intends to investigate whether the calibration software converges. When the same data is calibrated several times, differences in the determined gain factors between iterations should vanish.

The results are shown in figure 8.6. Here, a dataset of 225,000 events taken with SM-II was calibrated three times with a granularity of (0,0), i.e. the calibration was performed chamber-by-chamber. At this granularity level sufficient statistics were accumulated in layer 5, too. So this layer was included in the investigation. The procedure is explained in the following.
The raw data was reconstructed relying on a default OCDB, where the gain factors are uniformly set to 1. The reconstructed ESDs were then calibrated, the calibration software related to the same default OCDB. The output is a new database DB(1)[25] with the determined gain factors represented by the red dots in figure 8.6. Then, a second reconstruction pass was performed with the same set of raw data. This time, the reconstruction software took DB(1) into account. The new ESDs were calibrated again. As mentioned in chapter 7, it is possible to pass a previous DB to the calibration software. In a second calibration procedure, it updates the values, i.e. the software determines differences to the previous DB, adds the differences to the previous values and then stores the values in a new DB. Besides gain factors, values of the drift velocity were determined and used in the next iteration, too. The gain factors of this second DB(2) are represented by the green squares in figure 8.6. A third iteration was performed, with both reconstruction and calibration taking DB(2) into account. The blue triangles represent the determined gain factors.

Figure 8.6 shows that the calculated gain factors converge. The gap between first and second iteration is due to the fact that in the default OCDB, the drift velocity is set to $1\,\mathrm{cm}/\mu\mathrm{s}$, but for a typical drift voltage of $-1500\,\mathrm{V}$, in $ArCO_2$ the drift velocity is about $2\,\mathrm{cm}/\mu\mathrm{s}$. This affects the reconstruction in the first iteration. Tracklets might be not well determined. Fortunately, the shape of the gain is conserved and the gain factors are only shifted. Since a relative calibration is performed, wrong values of drift velocity usually do not sabotage a correct gain calibration, although this effect has to be taken into account when different runs are compared.
For chambers 15 and 29, values are not shown. This is because the high voltage was switched off in these chambers, and therefore no tracklets were found.

[25] With (1) standing for first iteration.

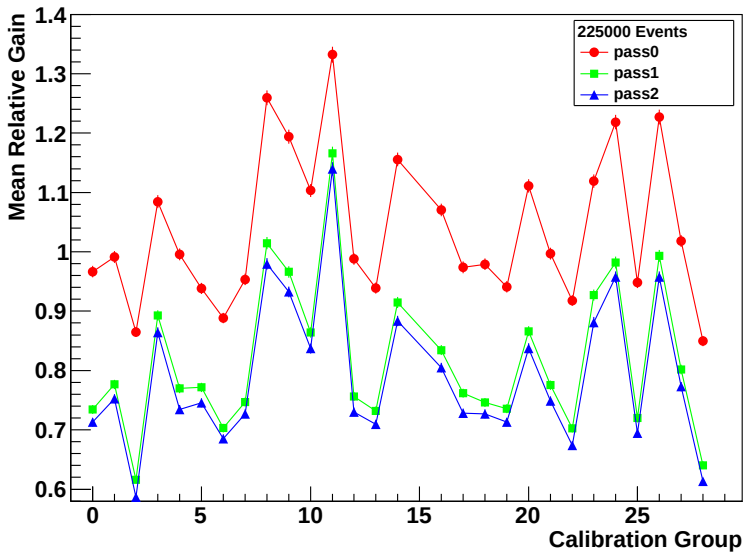

Figure 8.6: For three calibrations of the same raw data, calculated gain factors are shown. For pass 0, reconstruction and calibration were done with a default OCDB. For pass 1 and pass 2, reconstruction and calibration were performed with the previous DB created by the calibration software. In chambers 15 and 29, the high voltage was switched off, associated points are not drawn.

9 Gain Calibration of the TRD

In this chapter, the gain of the ALICE TRD readout chambers is investigated. The measurements were done with TRD supermodules in Münster, using the experimental setup described in chapter 6.

9.1 Gain as a Function of Anode Voltage

The gain of the TRD chambers is highly dependent on the applied anode voltage, as outlined in chapter 4. The anode voltage directly influences the number of electrons in the avalanche, thus the gas gain. From electrostatic calculations, it is expected that the gain increases exponentially with the anode voltage [ALI01]. Several measurements regarding this topic have already been carried out, but the gain has not been determined with the AliRoot calibration software before. The measurement will be explained and compared to previous ones.

9.1.1 Measurement of Gain as a Function of Anode Voltage

The cosmic ray data were taken with SM-VII. The cosmic trigger was set to coincidence mode, with the upper trigger placed above stack 3. The data for chambers 18-22 (stack 3, layers 0-4) were analyzed, layer 5 was left out due to the tracking problems mentioned in section 8.1. For this analysis, the calibration was carried out with (3,3) granularity, i.e. each chamber was subdivided into 64 calibration groups with 36 pads per group (see table 7.1). For 1400 V, 1450 V and 1500 V of anode voltage, the gain factors of each calibration group were determined with the calibration software.
Since it is possible to pass an arbitrary default OCDB to the calibration software, runs with different gas gain can be compared. Although the different groups are calibrated relatively to each other for a given run, the computed gain factors are also compared to previous signal amplitudes. In the default OCDB, an evenly distributed gas gain of 1 for a standard signal amplitude is stored. Therefore, changes in gain for different runs can be investigated.

9.1.1.1 Global Behaviour

Every line in the plot of figure 9.1 corresponds to one calibration group. The dots represent the calculated gain factors at three different anode voltages. Only calibration groups with sufficient statistics in every data point are plotted. If the statistics in a group are too low, the software sets the gain factor to the default value of 1. For this measurement, the cut was set to > 100 entries in order to perform a calibration. The dashed line indicates the mean of the plotted gain characteristics.
The errors of the data points in gain were estimated from the number of entries using equation 8.3. In the data, the number of entries per calibration group is mostly between 1000 and 2000, but values from 0 to 3000 appear. The error in voltage is well below 1 V and is not visible in the plots.
Since the data points are strongly correlated for a given calibration group, the standard deviation of the data points would strongly overestimate the error of the mean. Thus, the mean of the error bars of all measurements was taken as error of the mean gain.

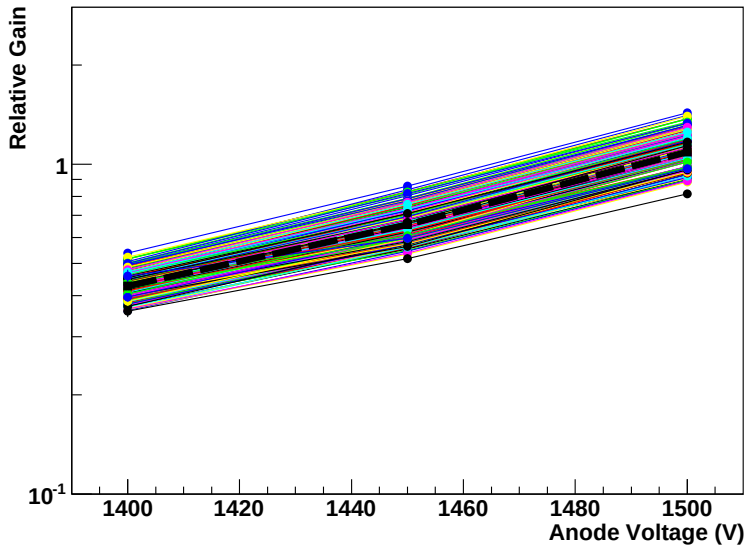

Figure 9.1: Gain as a function of the applied anode voltage for 5 chambers of SM-VII. The dots indicate gain factors calculated with the calibration software. The lines correspond to different calibration groups. The dashed line represents the mean.

Looking at figure 9.1, the increase of gain in dependence of the anode voltage is slightly faster than exponential. The deviation from a perfect exponential behaviour can be explained by sagging of the anode wires towards the grounded pad

plane due to electrostatic forces [ALI01]. Nevertheless, the mean gain of all calibration groups has been fitted with an exponential function, figure 9.2 shows the result. The following function has been found:

$$g(U) \;=\; \exp\left\{(-14.083 \pm 0.497) + (9.438 \cdot 10^{-3} \pm 3.40 \cdot 10^{-4}) \cdot U\right\} \;, \qquad (9.1)$$

with $\chi^2/\mathrm{nDoF} = 2.26$ and covariance($p0$,$p1$) $= -1.6 \cdot 10^{-3}$.

The relative increase in gain for an increase of 1 V in anode voltage has been calculated with equation 9.1, it is:

$$\frac{\mathrm{d}g}{\mathrm{d}U} \;=\; (0.95 \pm 0.09)\,\frac{\%}{\mathrm{V}} \quad \text{for } \Delta\mathrm{U} \;=\; +1\,\mathrm{V}\;. \qquad (9.2)$$

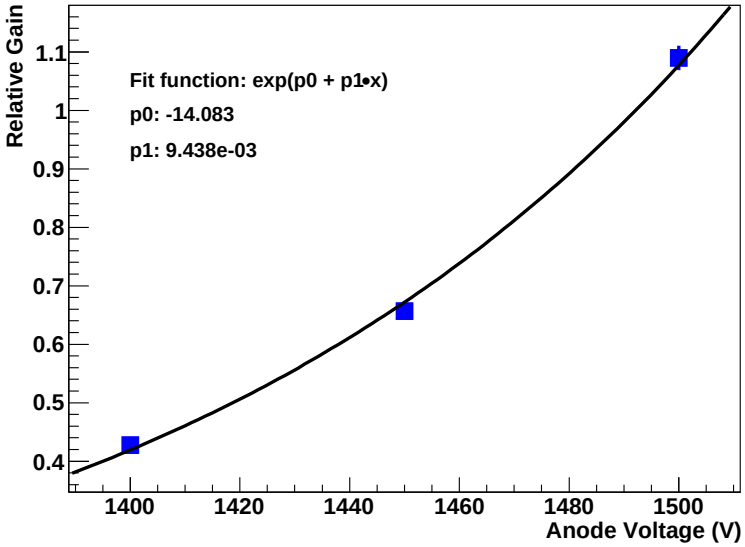

Figure 9.2: Mean relative gain of 384 calibration groups of SM-VII (blue dots), and exponential fit (black line).

9.1.1.2 Local Differences

In this section, it is investigated whether the change in gain depends on the position of the calibration group in the chamber. The expectation is that the changes in gain should be homogeneous inside a chamber.
As mentioned above, for this calibration every chamber has been subdivided into 64 calibration groups, each with 18 pads in column direction and 2 pads in row

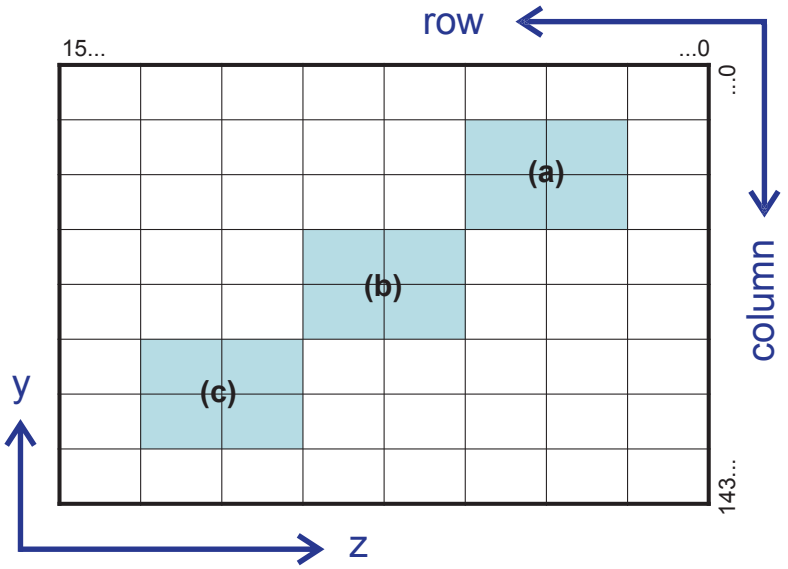

Figure 9.3: Division of a C1 readout chamber into calibration groups at a granularity of $(nz, nrphi) = (3, 3)$. In this case, 36 pads belong to each calibration group. Shaded areas indicate investigated parts: a) column 18-53, row 2-5, b) column 54-89, row 6-9, c) column 90-125, row 10-13.

direction. In order to investigate changes in gain for different parts of a chamber, the calculated gain factors alongside the diagonal of the chambers were compared in the following way:

First of all, calibration groups at a chamber border were left out because often there are not enough entries in a group. The area covered by the residual 36 calibration groups was subdivided into nine areas, each composed of four calibration groups. Alongside the diagonal between column 18, row 2 and column 125, row 13, at three different positions the mean of four adjacent groups was calculated. Figure 9.3 sketches these positions. Groups of subsequent layers at the same position were summed. In the plot in figure 9.4, the red dots represent the mean gain factor of the calibration groups located between columns 18-53 and rows 2-5. The green squares represent the mean of groups between columns 54-89 and rows 6-9, i.e. the centre of the chambers. The blue triangles represent the mean of groups between columns 90-125 and rows 10-13. Groups with less than 100 entries in one ore more measurements were once again left out. The errors were calculated using the Gaussian law of error propagation.

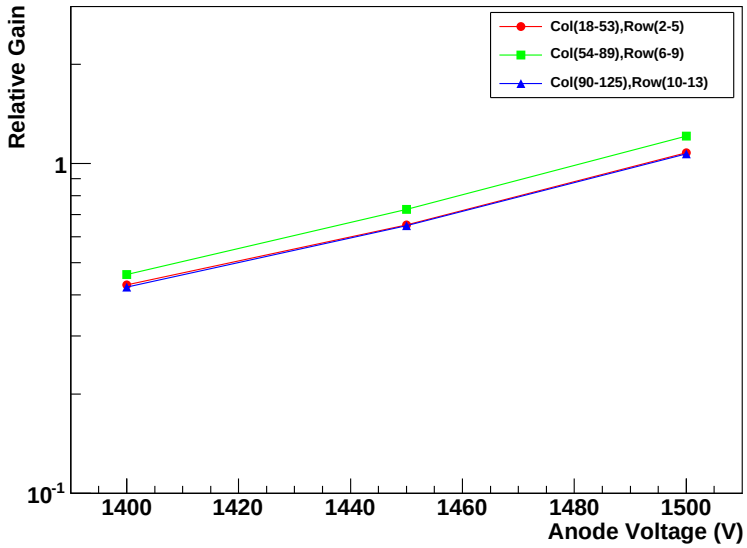

Figure 9.4: Gain as a function of the applied anode voltage for 5 chambers of SM-VII. The markers represent mean values of calibration factors of calibration groups at the positions given in the legend.

Obviously, the change in gain for an increase of the anode voltage is in a good approximation independent of the pad position in the chamber because no differences in the slopes can be observed. Nevertheless, the gain in the middle of the chambers is slightly higher than at the edges. This can be explained by small deformations of the chambers, since the measurements were done with a slight underpressure in the chambers relative to the atmosphere. A detailed explanation is given in section 9.2.

9.1.2 Comparison to Previous Measurements

The changes of gain in the TRD in dependence of the applied anode voltage have been investigated several times before. In the year 2001, it was done by electrostatic calculations in the *Technical Design Report* of the ALICE experiment [ALI01]. In 2005, S. Freuen investigated the gain of single TRD chambers for his diploma thesis [Fre05], and in 2008, P. Reichelt investigated the same subject for his bachelor thesis [Rei08], [AHR08]. In both theses, radioactive sources were used, and the gain was determined by measuring the current at the anode wires. In 2009, the PhD thesis of R. Bailhache described measurements with cosmic rays done in Münster [Bai09a]. In this case, an early version of the calibration software was used, however much

less data were calibrated than in the analysis of section 9.1.1. The signals of a whole SM were integrated. The measurements are summarized in table 9.1.

Work	Voltage Range (V)	Gas Mixture (%)	Measurand
Own	1400 - 1500	$Ar/CO_2(83/17)$	energy deposit
[ALI01]	1350 - 1500	$Xe/CO_2(85/15)$	electrostatic calculations
[Fre05]	1350 - 1500	$Ar/CO_2(85/15)$	anode current
[Rei08]	1450 - 1600	$Ar/CO_2(70/30)$	anode current
[Bai09a]	1420 - 1600	$Ar/CO_2(63/37)$	energy deposit

Table 9.1: Several measurements of gain in dependence of anode voltage for ALICE TRD chambers.

The measurements used different methods and therefore gave different units of the gain. When the anode wire current is measured, the absolute gain (of the order $\sim 10,000$) is determined. Relative gain calibrations give gain factors ~ 1. In order to compare the results (see figure 9.5) the gains have been normalized to give 1.0 for an anode voltage of 1500 V. Uncertainties have been estimated if not given in the publications.

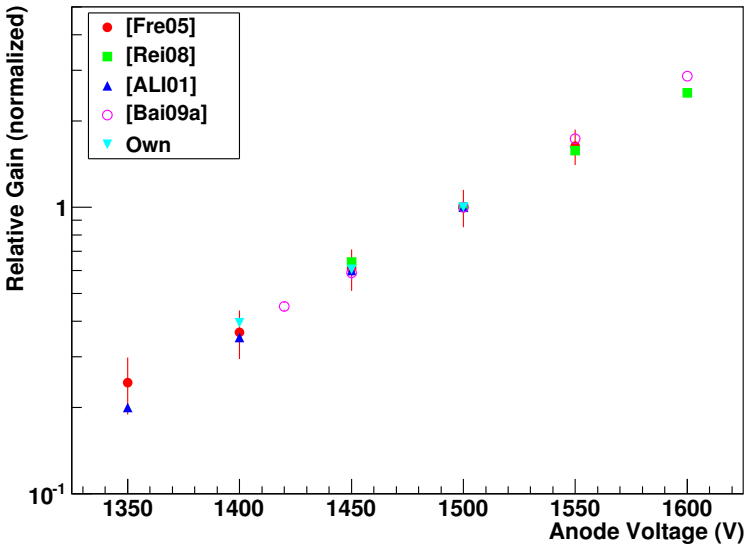

Figure 9.5: Gain in dependence of anode voltage, each measurement normalized to a gain of 1.0 for 1500 V.

The measurements were done in different voltage ranges, and due to the fact that the gain is exponentially dependent on the anode voltage, measurements cannot

be linearly extrapolated to other voltage ranges. So, in order to compare results, the normalized values of each measurement have been fitted with an exponential function. According to the calculations in section 9.1.1.1, for each measurement the percentage variation in gain for an increase of 1 V in anode voltage has been calculated with the associated fit function. Figure 9.6 presents the results, errors were calculated from errors and covariances computed for the fit functions.

The calculation of the relative change in gain for the measurement of [Fre05] gives a huge error of ± 4.3. This is due to the fact that quite large errors are given for the data points of this measurement. In fact, looking at figure 9.5, it seems that the error bars are correlated and that the errors were overestimated.
In the range of their accuracy, the calculated gain variations are all of the same size. This is a positive test for the accuracy of the calibration software used in this thesis, since except for [Bai09a], all compared publications determined the gain variations in different ways.

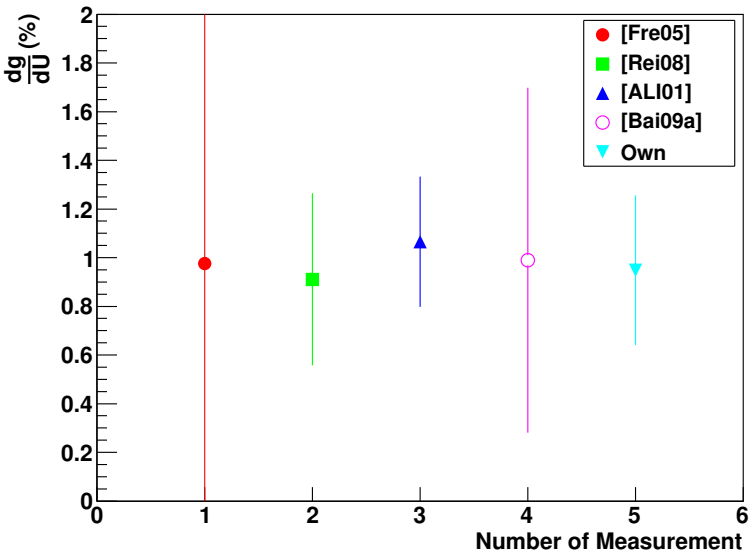

Figure 9.6: Percentage increase of gain for an increase of 1 V in anode voltage, calculated with the fit functions to the measurements.

9.2 Gain in Dependence of Differential Pressure

When the pressure inside the gas volume of the ROCs is not equal to the atmospheric pressure, the resulting pressure gradient could cause a bending of the

ROCs. An overpressure inside the chambers compared to the atmospheric pressure can induce the pad plane to bend outwards, away from the anode wires. The gas gain would decrease. A lower pressure inside the ROCs could lead to an increasing gas gain, respectively.

9.2.1 Measurement of Gain in Dependence of Differential Pressure

With the SM-VII, gain variations in dependence of the differential pressure were investigated. The data were taken in coincidence trigger mode, with the upper trigger placed above stack 3. With the gas system installed in Münster, the differential pressure can only be monitored for one double layer at a time . Two ROCs in layer 0 and layer 1 of stack 3 were examined. As in the analysis presented in section 9.1, the calibration was performed with (3,3) granularity, at which a chamber is subdivided into 64 calibration groups, each consisting of 2 rows and 18 columns. At this granularity level, it took about 1.5 hours per measurement to accumulate enough statistics.
The pressure in a double layer can be changed by adjusting the gas flow to the ROCs. A pressure sensor at the outlet of the double layer monitors the differential pressure between the gas volume inside the chambers and the atmosphere, $\Delta P =$ [(pressure in ROCs)-(atmospheric pressure)]. Four runs with ΔP(mbar) = (-1.4, -0.7, -0.1, +1.1) were analyzed.

9.2.1.1 Changes of the Gain Profiles

Figure 9.7 shows changes of the gain for various values of the differential pressure in detector 18 (ROC in stack 3, layer 0) and figure 9.8 shows the behaviour in detector 19 (ROC in stack 3, layer 1). In the plots, square areas represent the calibration groups. In figures 9.14 and 9.15, the gain factors were integrated over the columns or the rows, respectively. Here, results for different pressure gradients are indicated by coloured lines.

As expected, the gain decreases with increasing overpressure in the chambers. This effect seems to be strongest in the centre of the ROCs. The following conclusions are obtained from the plots:

- Bending of the chambers due to changes of the differential pressure has a big effect on the gas gain. Besides a shift in height, the profile of the gain might even be inverted as can be seen in figure 9.7.

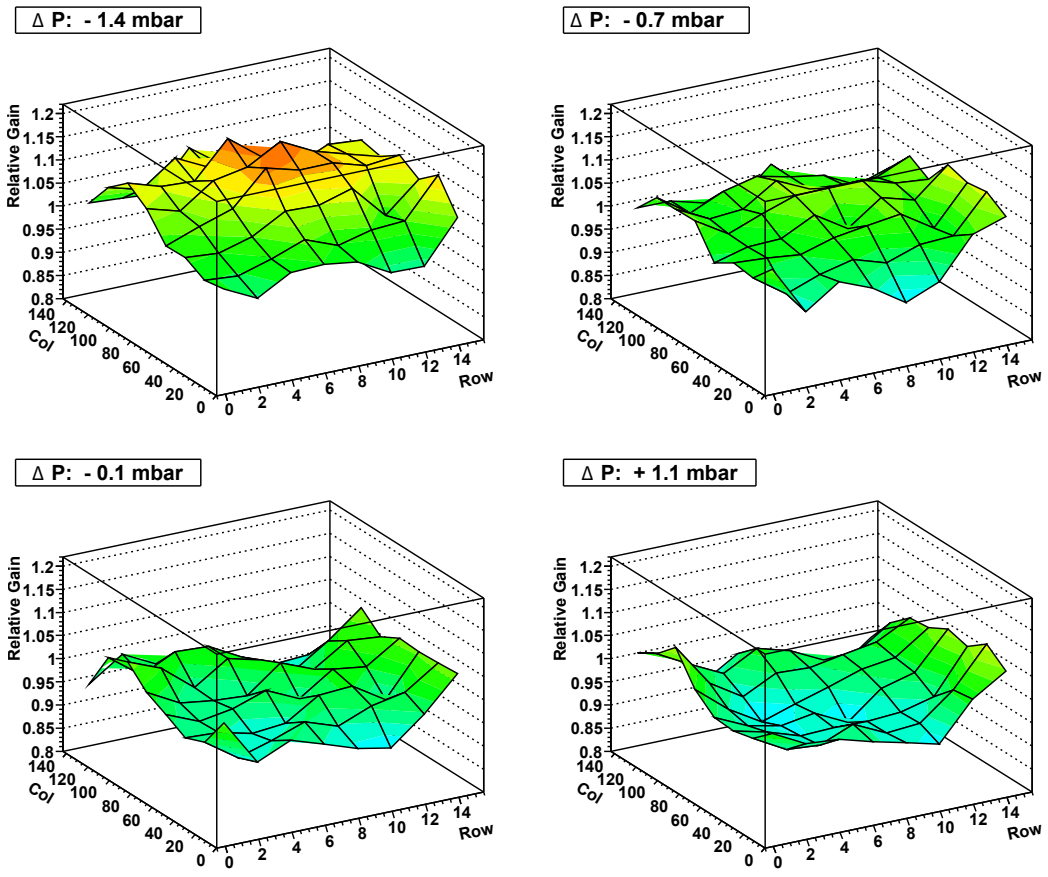

Figure 9.7: Gain profiles for detector #18 (stack 1, layer 0) of SM-VII, square areas represent a calibration group. Shown are results for different pressure gradients.

- For the two examined chambers, the gain profiles change with the applied pressure gradient in a unique way. A global correction function $f(\Delta P)$ that would allow to determine the gain independently of the differential pressure cannot be found.
- In order to compare results of different runs, it is crucial to apply the same differential pressure to the ROCs. For some chambers, gain profiles were also determined during their production phase. For these measurements, radioactive materials served as particle sources. The gain was calculated from the current at the anode wires. Unfortunately, the differential pressure had not been recorded. However, the gain profile computed for detector #19 (figure 9.8) at 1.1 mbar overpressure is similar in shape and height to the profile determined in the previous measurement for this ROC [Sch09], see figure 9.9. For detector #18 no reference data is available.

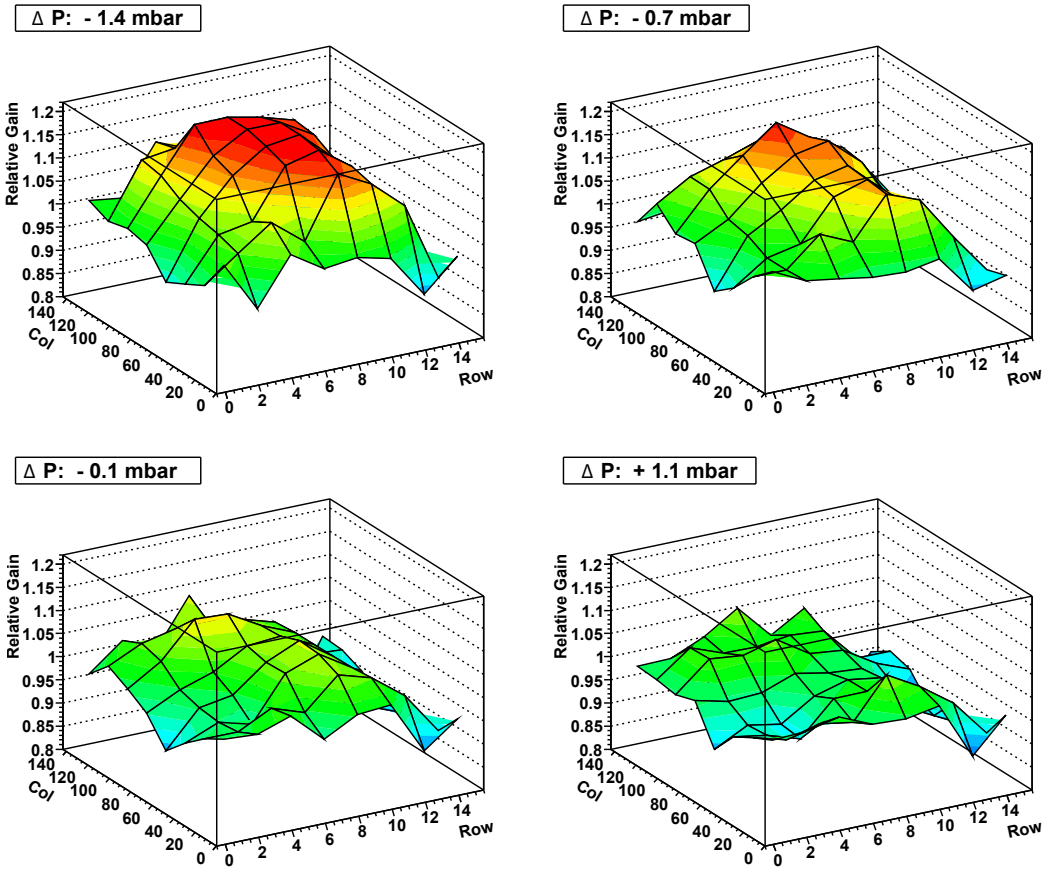

Figure 9.8: Gain profiles for detector #19 (stack 1, layer 1) of SM-VII, square areas represent a calibration group. Shown are results for different pressure gradients.

9.2.1.2 Local Differences

If bending of the pad plane is the reason for changes of the gain profiles, the effect should be strongest in the middle of the ROCs. Gain factors for different areas of the two examined ROCs are plotted to investigate on this. According to the analysis described in 9.1.1.2, calculated gain factors alongside the chambers diagonal were compared. Again, calibration groups at a chamber border were left out because of low statistics. Groups in column 18-53, row 2-5 are in the bottom right corner of a chamber, groups in column 90-125, row 10-13 are in the upper left corner and groups in column 54-89, row 6-9 are in the centre of a chamber. The positions are sketched in figure 9.3.
Since two layers were investigated, values of eight groups per area are plotted in figures 9.10, 9.11 and 9.12. In these figures, a coloured line represents data of one

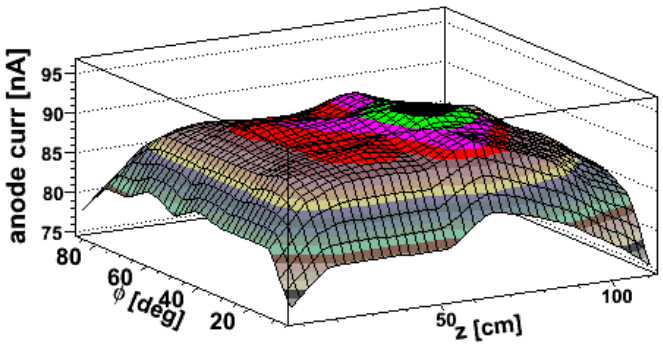

Figure 9.9: Gain profile for detector #19, measured during the production phase [Sch09]. z-direction corresponds to negative row-direction, φ-direction corresponds to the column direction.

calibration group. The errors of the gain factors were calculated from the numbers of entries using equation 8.3. For the analyzed ROCs, the numbers of entries per calibration group were around 1500, but values from 250 to 2500 appeared. The errors of the differential pressure are given by the standard deviation of the monitored pressure values. The dashed black line represents the mean of the plotted calibration groups. Here, the error bars were derived using the Gaussian law of error propagation. In a given area, the gain shows a uniform behaviour.

In figure 9.13, the means of the different areas are plotted. Obviously, the effect of chamber bending on the gain caused by changes of the differential pressure is strongest in the middle of the chambers. During the design phase of the TRD, electrostatic simulations investigated changes in gain due to chamber bending. For an overpressure of 1.0 mbar, a decrease in gain of 7 % compared to 0 mbar pressure difference is predicted for the centre of a chamber [ALI01]. This fits well to the mean of the measured gain variations in the middle of the chambers, given in table 9.2 and shown in figure 9.11. With ~ 5.7 % for a slightly larger change in pressure of $\Delta P = 1.2$ mbar, the effect actually seems to be a bit smaller. On the other hand it has to be considered that an area of 144 pads is analyzed instead of the exact chamber centre.

	ΔP	Gain Factor	Percent
	-0.1 mbar	1.02503	100.000 %
	$+1.1$ mbar	0.96679	94.318 %
Δ	1.2 mbar	0.05824	5.682 %

Table 9.2: Mean gain factors of calibration groups in the middle of the ROCs.

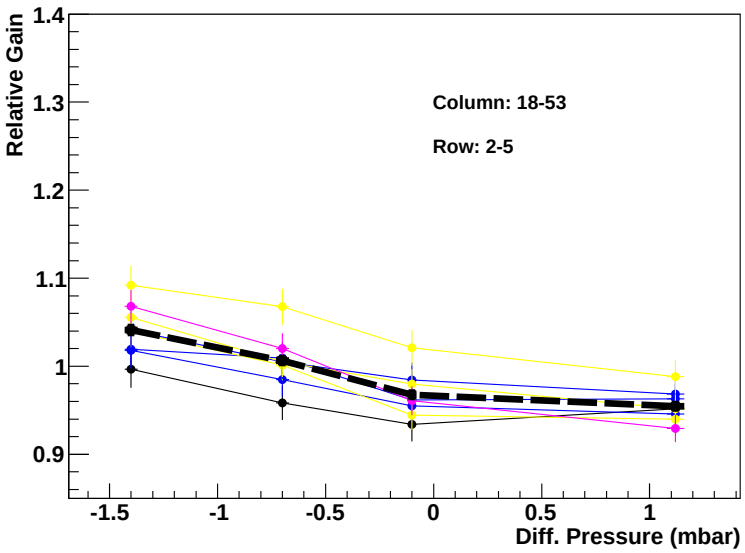

Figure 9.10: Gain in dependence of the differential pressure for calibration groups in column 18-53, row 2-5. Coloured lines indicate calibration groups in SM-VII, detectors #18 and #19. The black dashed line indicates the mean.

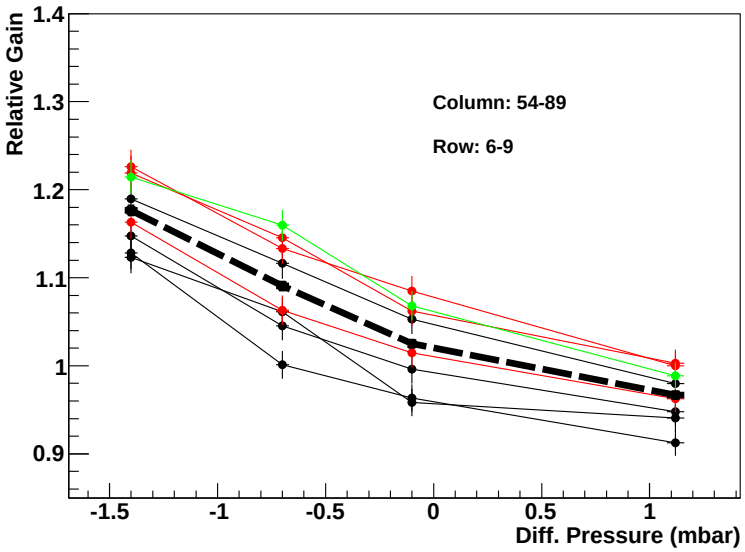

Figure 9.11: Gain in dependence of the differential pressure for calibration groups in column 54-89, row 6-9. Coloured lines indicate calibration groups in SM-VII, detectors #18 and #19. The black dashed line indicates the mean.

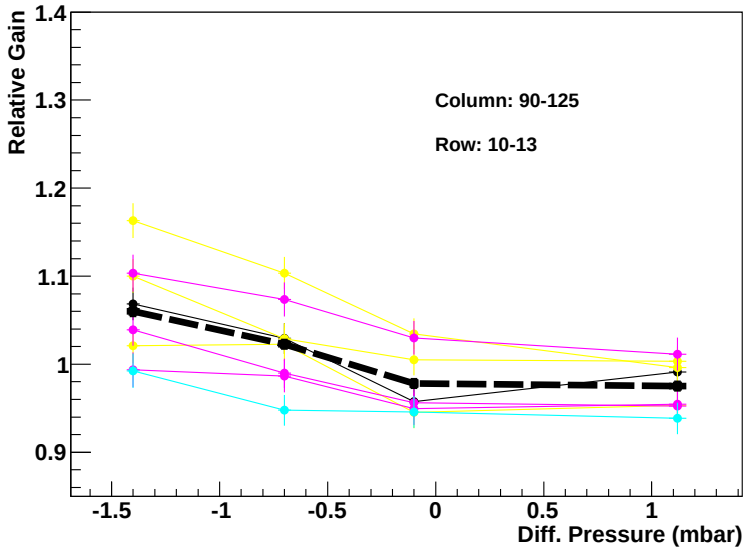

Figure 9.12: Gain in dependence of the differential pressure for calibration groups in column 90-125, row 10-13. Coloured lines indicate calibration groups in SM-VII, detectors #18 and #19. The black dashed line indicates the mean.

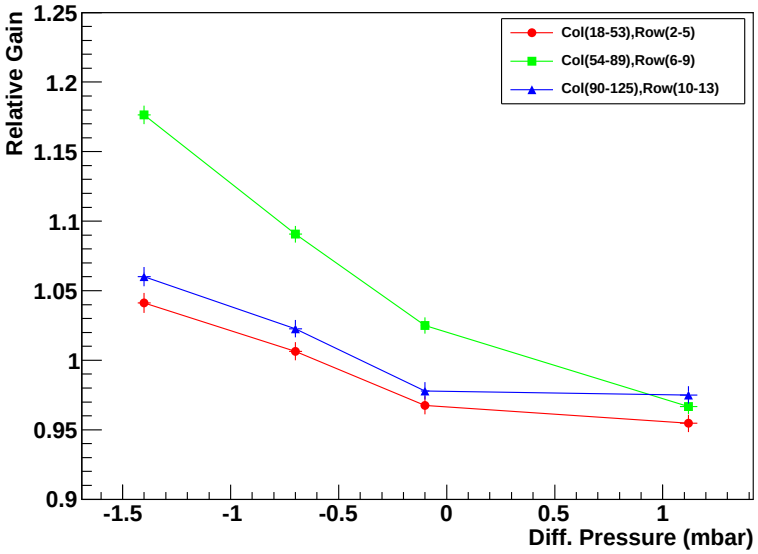

Figure 9.13: Gain in dependence of the differential pressure for different areas of the ROCs. The lines represent the mean of eight calibration groups at a given position. The data was taken with SM-VII, detectors #18 and #19.

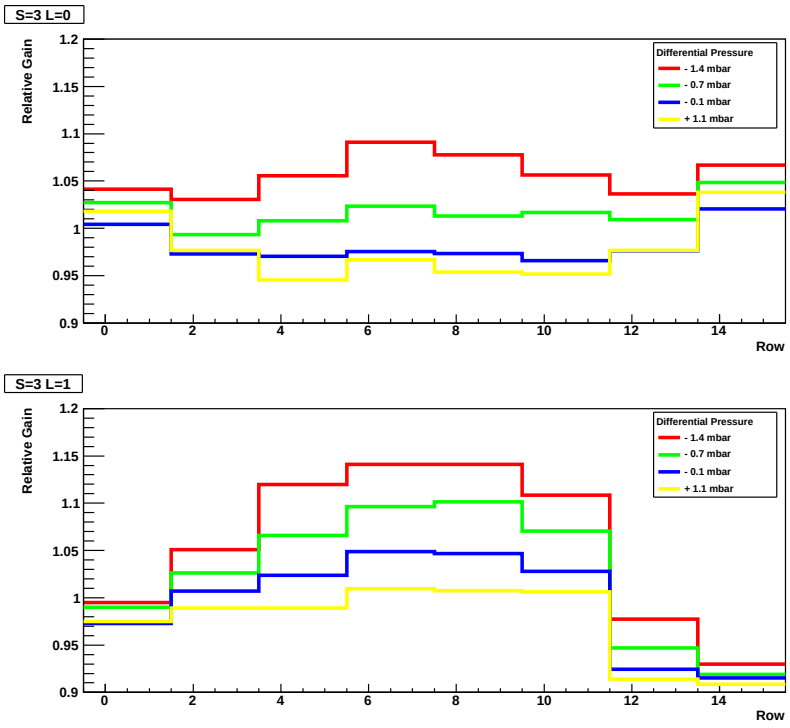

Figure 9.14: Gain profiles for different relative pressures. For each row, the mean of all columns at this position is plotted. Upper panel: SM-VII detector #18, lower panel: SM-VII detector #19.

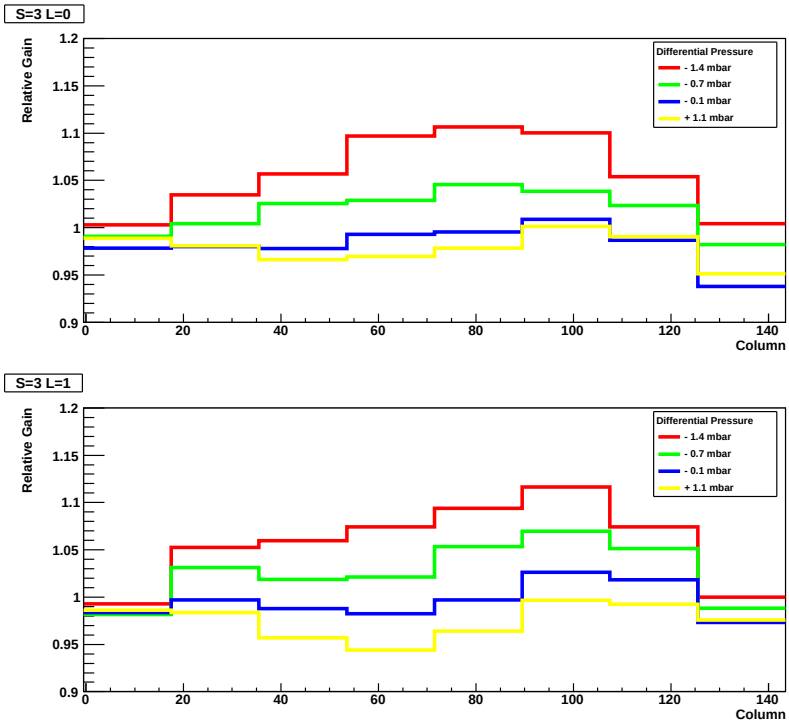

Figure 9.15: Gain profiles for different relative pressures. For each column, the mean of all rows at this position is plotted. Upper panel: SM-VII detector #18, lower panel: SM-VII detector #19.

9.3 Gain Correction in the MCM

When the TRD is used as a trigger, gain correction becomes necessary at an early stage, even before tracklets and tracks are calculated. As already mentioned in chapter 4, a gain filter is implemented in the MCMs in order to perform a first gain correction online. Within a certain range, it is possible to adjust the signals of the ADCs in a way that a uniform gain is provided by each MCM. The gain factors of every pad need to be known in order to determine the filter values for the ADCs. Those values can be obtained from the OCDB created by the calibration software. In this chapter, the procedure of gain correction within the MCMs will be explained.

9.3.1 Architecture for Gain Correction

In the MCMs, the gain filter stage is implemented between the pedestal correction and the tail cancellation[26].
Figure 9.16 sketches the logical circuit diagram of the gain filter. For a given ADC, the signals from the pedestal correction output are multiplied by the gain correction factor of this ADC. Afterwards, a pedestal correction additive is added. As mentioned before, the pedestal is changed by the multiplication as well. The addition of individual values to the signals again provides a uniform pedestal. Before reaching the input of the tail cancellation filter, the signals are passed to a multiplexer unit where it is possible to bypass the gain correction.

Presented already as equation 4.2, gain correction within an MCM is described by

$$O_n(t) \;=\; \gamma_n \cdot I_n(t) \;+\; \varrho_n \;, \tag{9.3}$$

where n represents one of the 21 ADC channels. The input signal $I_n(t)$ from the pedestal correction is multiplied with a gain correction factor γ_n. After the pedestal correction ϱ_n has been added, the output signal $O_n(t)$ is passed to the tail cancellation filter.

One has to consider that γ_n and ϱ_n are stored as binary values in the MCMs. Furthermore, these binary values are approximated by integer numbers in order to load them into the electronics (see section 9.3.3). Ruled by the numbers of binary digits, both values are restricted to certain ranges. Let a subscripted 10 denote the decimal representation (base-10) of the gain correction factor and pedestal additive, and a subscripted 2 denote their binary representations (base-2), then it is [L$^+$05]

$$\gamma_{2,n} \;=\; (\gamma_{10,n} - 0.875) \cdot 2^{11} \;; \qquad 0.875 \leq \gamma_{10,n} \leq 1.125 - 2^{-11} \tag{9.4}$$

for the gain correction factors and

$$\varrho_{2,n} \;=\; (\varrho_{10,n} - 0.0) \cdot 2^{2} \;; \qquad 0.0 \leq \varrho_{10,n} \leq 15.75 \tag{9.5}$$

for the pedestal additives. Considering these restrictions, it is $0 \leq \gamma_{2,n} \leq 511$ and $0 \leq \varrho_{2,n} \leq 63$.

[26] See also section 4.6 for explanations.

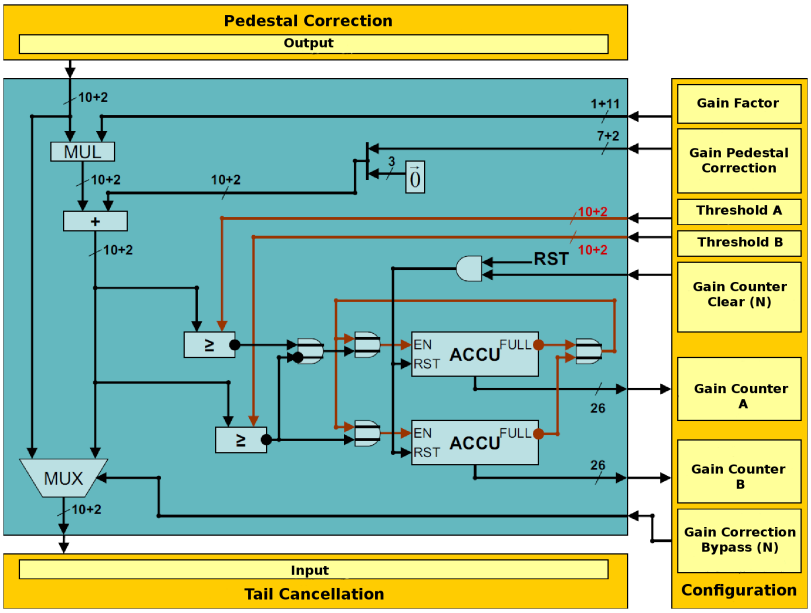

Figure 9.16: Gain filter stage of an MCM [Gut02].

As outlined in section 4.6, the number of ADC channels is bigger than the number of pads in the TRD. Every MCM has 18 PASA channels, each connected to one pad. The ADC channels 2-19 are connected to these PASA channels.

In addition, to inhibit border effects, e.g. loss of acceptance, ADC channels 0,1 and 20 are connected to PASA outputs of neighbouring MCMs. Figure 9.17 sketches the situation. Channel 20 is connected to the PASA output 0 of the next MCM in positive y-direction (negative column direction), channels 0 and 1 are connected to PASA outputs 16 and 17 of the other neighbouring MCM. At the chamber borders, interconnected channels without a corresponding pad are masked out.

Two things have to be kept in mind:

- In the OCDB, the gain factors of all pads are stored, corresponding to the PASA inputs in figure 9.17. When creating a gain table for the ADC channels, one has to take care that the ADC filter values are matching the correct pad gains. Wherever possible, the AliRoot classes `AliTRDgeometry` and `AliTRDfeeParam` were used to calculate the correct linkage.

- With the described method, a uniform gain is only generated within an MCM, i.e. neighbouring MCMs will provide different gains. For double connected PASAs (e.g. for pad columns 17, 35 and 36), the PASA signal will look

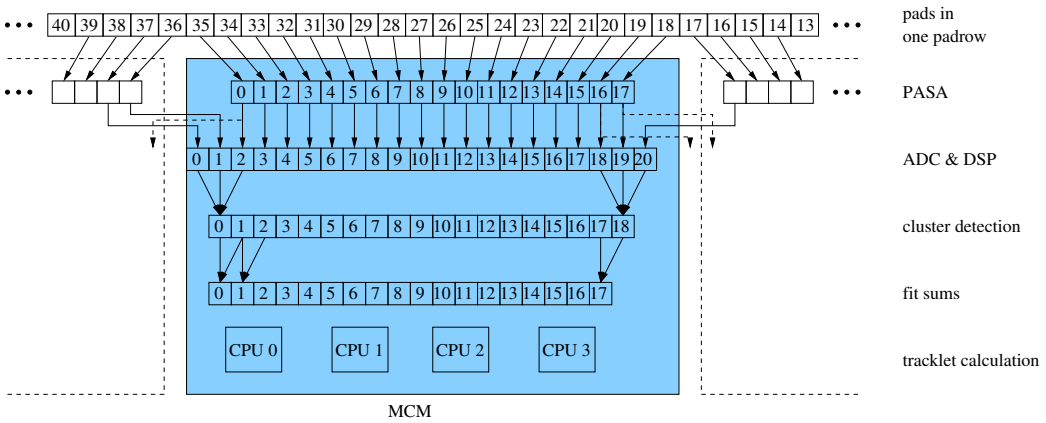

Figure 9.17: Mapping of channels in an MCM [Kle08]. Note that channel numbering is opposite to pad numbering.

different in the two MCMs when gain filtering is applied. Since these values are used for online calculations only, this should not affect any offline analysis.

9.3.2 Tests of the MCM Gain Correction

The gain correction factors and pedestal additives are calculated from the OCDB gain factors in the following way:

Except for the ROC borders, every MCM processes signals from 21 pads. For each MCM, the pad with the lowest gain factor is selected and the corresponding ADC channel is corrected with $\gamma_{max} = (1.125 - 2^{-11})$, the highest possible correction factor. The other 20 ADC channels receive correction factors $\leq \gamma_{max}$, so that every ADC of the MCM delivers the same signal amplitude for a given input signal $S(t)$:

$$\gamma_i \cdot S(t) \;=\; \text{const} \qquad \forall\, 0 \leq i \leq 20\ . \tag{9.6}$$

The γ factors for ADCs at ROC borders without corresponding pads are arbitrarily set to 0.875.

A pedestal of 10.0 was chosen before as output of the pedestal filter stage. Since ϱ_n is an additive, the pedestal can only be raised in the gain filter. This is an important point. In order to obtain a pedestal of 10.0 after the gain filter stage, the settings of the pedestal filter have to be adjusted to give a smaller pedestal than

in absence of gain filtering. For this analysis, a value of 8.0 has been chosen as output of the pedestal filter. The additive ϱ_n is determined by the gain correction factor γ_n in each ADC:

$$\varrho_{10,n} \;=\; \{(1.0 - \gamma_{10,n}) \cdot 8.0 \;+\; 2.0\} \; . \tag{9.7}$$

9.3.2.1 Effects of Limited Range

With $0.875 \leq \gamma \leq 1.125 - 2^{-11}$, gain correction is limited to gain variations of ± 12.5 % within an MCM. For the run number 2003 taken with SM-I, it was investigated how often gain variations exceed the possible correction range, some results are presented in figure 9.18. A calibration with (4,5) granularity has been performed, i.e. each calibration group comprises 4 adjacent pads in column direction within one pad row. The upper left panel presents the distribution of the lowest γ factors. For each MCM, one entry is added for the ADC with the highest gain and thus the lowest correction factor. For this run, 4.71 % of the ADCs and 10.5 % of the MCMs have correction factors smaller than 0.875.
The bottom left panel presents the second lowest γ for each MCM. Leaving out the ADCs[27] with the lowest correction factors does not solve the problem, gain variations appear to be actually too big for some MCMs.
The upper right panel presents the ratios of the lowest and highest correction factors, again for each MCM. Since the highest γ has been fixed to ≈ 1.125 for every MCM, with the given range, the ratios should not be smaller than $0.\overline{7}$ (blue line).

In the plots discussed above we have already seen that some γ factors are too small, that is why some ratios exceed the range in this plot. The peak at 1.0 comes from MCMs with low statistics. When there are less than 100 entries in a calibration group, the gain is set to 1.0. When all groups associated with one MCM have too low statistics, all correction factors are equal. Consequently the ratio of highest and lowest γ is 1. This is the case for more than 350 MCMs.
An important point is the accuracy of the calibration procedure, decreasing with $1/\sqrt{n}$ (equation 8.2). When the number of entries is bigger than 100 but still small, the relative error of the determined gain factors is approximately twice as big as for more than 1000 entries. Furthermore, the previously discussed problems regarding the tracking software to find tracklets in layer 5 might produce additional errors. In order to investigate whether larger numbers of analyzed tracklets improve the gain correction within the MCM, cuts on the number of entries were done. In the bottom right panel of figure 9.18, a cut was set to 600 entries per calibration

[27] At the given granularity, each four pads in column direction have the same gain factors.

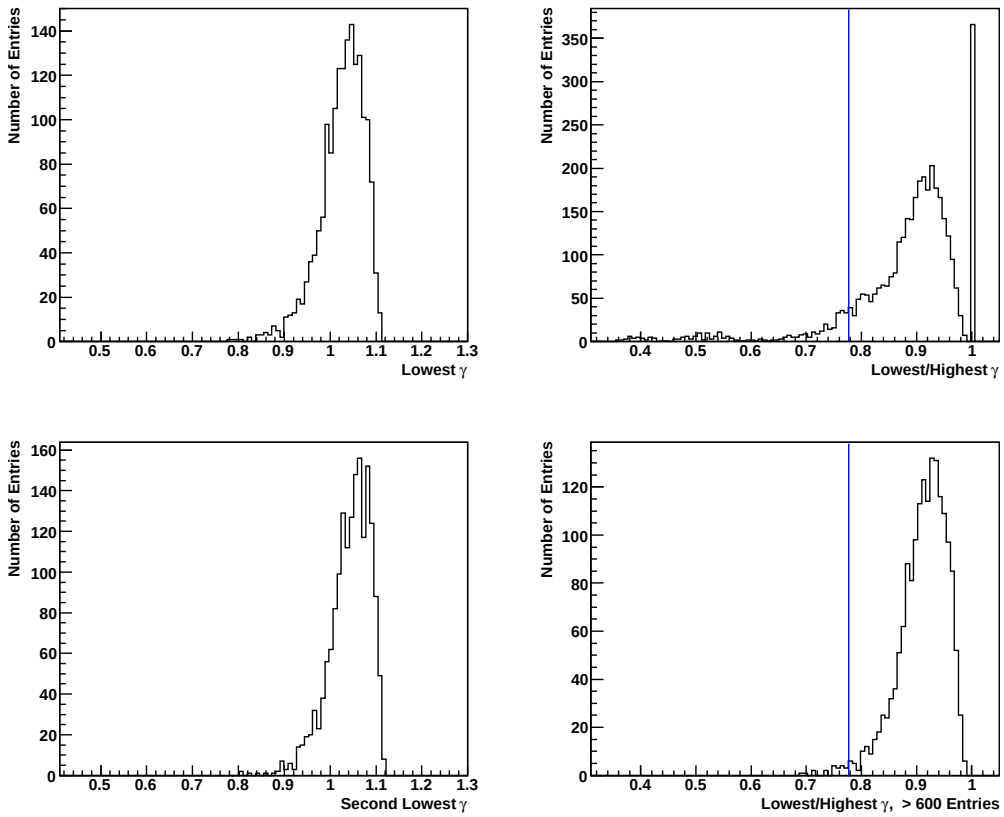

Figure 9.18: Distributions of ADC gain correction factors γ for the run 2003. Top left panel: lowest γ per MCM, bottom left panel: second lowest γ per MCM. Top right panel: ratios of lowest and highest γ, bottom right panel: ratios of lowest and highest γ, given more than 600 entries per calibration group.

group. If one or more groups associated with an MCM had less than 600 entries, the whole MCM has been left out. It turns out that larger statistics improve the online gain correction significantly. But still, for ~ 0.7 % of the MCMs, the range of gain variations remains too big. The residual number of MCMs out of range does not vanish even if much higher cuts are applied. For those MCMs, the gain tables will have to be adjusted, e.g. ADC correction factors out of range could be changed to the next possible value.
Regarding runs with other SMs, the results look very similar, but a cut on the number of entries cannot be made as too small statistics were accumulated.

We have just seen that the basis for reasonable MCM gain tables is a profound gain calibration for every pad of the SM. Unfortunately, several problems occurred when this was tried in Münster:

- With the experimental setup in Münster, a sufficient number of entries cannot be accumulated at the chamber borders (see chapter 6). Too low statistics in a calibration group leads to a bad accuracy of the gain calibration. Because the energy loss is Landau distributed, the software tends to compute gain factors that are too high for small numbers of entries. It is observed that pads with too low correction factors γ (i.e. too high gains) are mostly located at the ROC borders.
- The highest possible granularity for gain calibrations performed in Münster is (4,5), i.e. the resolution is limited to four pads in column direction. Given the rate of cosmic events, a pad-wise calibration would require about two to three days of uninterrupted measurement (see chapter 6). This would collide with any assembly schedule. Besides, even for such a long term measurement the number of entries would still be very unevenly distributed in the ROCs, with too low statistics at the borders.
- The tracking software finds almost no tracklets in layer 5. The reason for this is under investigation but not solved until now. Thus, unfortunately no reliable gain factors can be determined for the pads of this layer.

9.3.2.2 Example of MCM Gain Correction

Regardless of the difficulties discussed above, the procedure of MCM gain table generation has been tested with data from run 2003. Figure 9.19 shows the relative gain factors for every pad of SM-I as determined by the calibration software. Each panel represents one layer, again the huge gain values in layer 5 are due to tracking problems.

In figure 9.20 the product of relative gain factors and ADC correction factors ($g \cdot \gamma$) is shown for every pad. Thin black lines indicate MCM borders. It can be seen that a uniform gain is achieved within the range of an MCM.

In the following, it is investigated how steps in gain between neighbouring pads of different MCMs change when MCM gain correction is applied. For several quantities, means and associated standard deviations have been calculated in order to determine changes in the distributions between gain factors g and corrected ADCs $(g \cdot \gamma)$ (1), changes in the step between gains Δg and corrected ADCs $\Delta(g \cdot \gamma)$, both

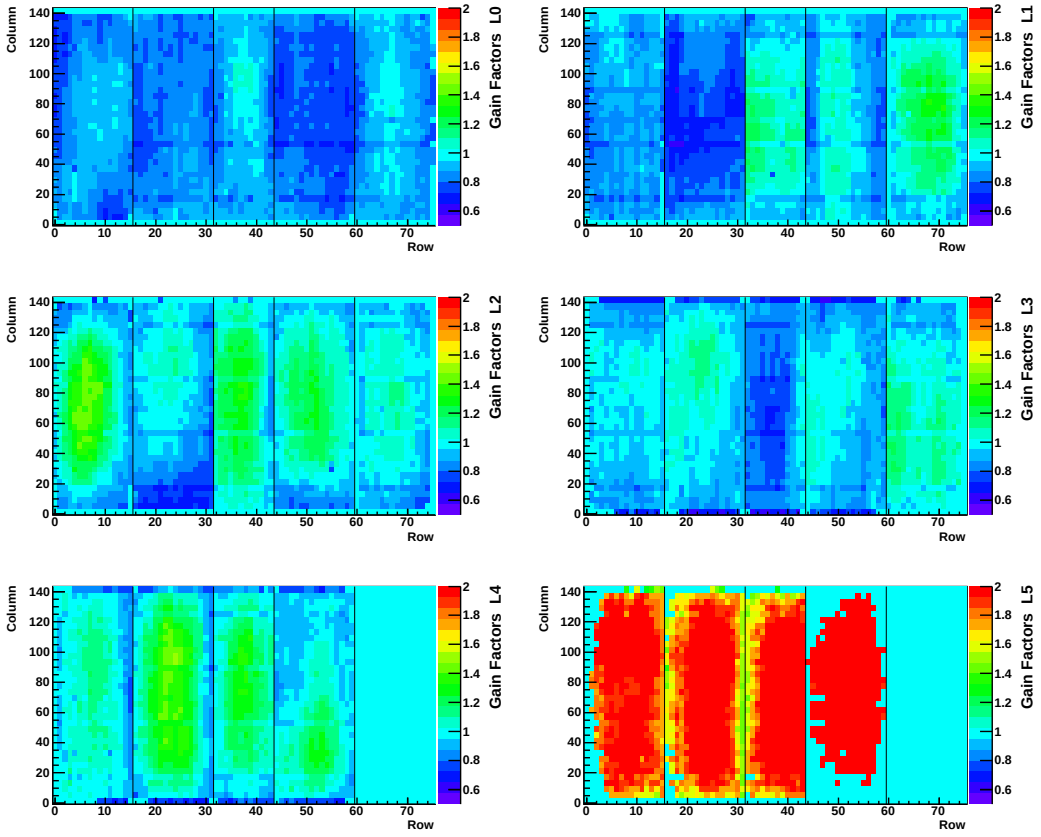

Figure 9.19: Gain factors for pads in SM-I, determined with data from run 2003.

for adjacent pads in column direction (2) and row direction (3). Results for pads in layer 5 were not taken into account. The following values were calculated:

M_{1a}	=	mean gain g of all pads,
σ_{1a}	=	associated standard deviation,
M_{1b}	=	mean $(g \cdot \gamma)$ of all MCMs,
σ_{1b}	=	associated standard deviation,
M_{2a}	=	mean Δg in column direction of pads at MCM borders (e.g. pad column 17-18),
σ_{2a}	=	associated standard deviation,
M_{2b}	=	mean $\Delta(g \cdot \gamma)$ in column direction between neighbouring MCMs,
σ_{2b}	=	associated standard deviation,
M_{3a}	=	mean Δg in row direction for all pads,
σ_{3a}	=	associated standard deviation,
M_{3b}	=	mean $\Delta(g \cdot \gamma)$ in row direction for neighbouring MCMs,
σ_{3b}	=	associated standard deviation.

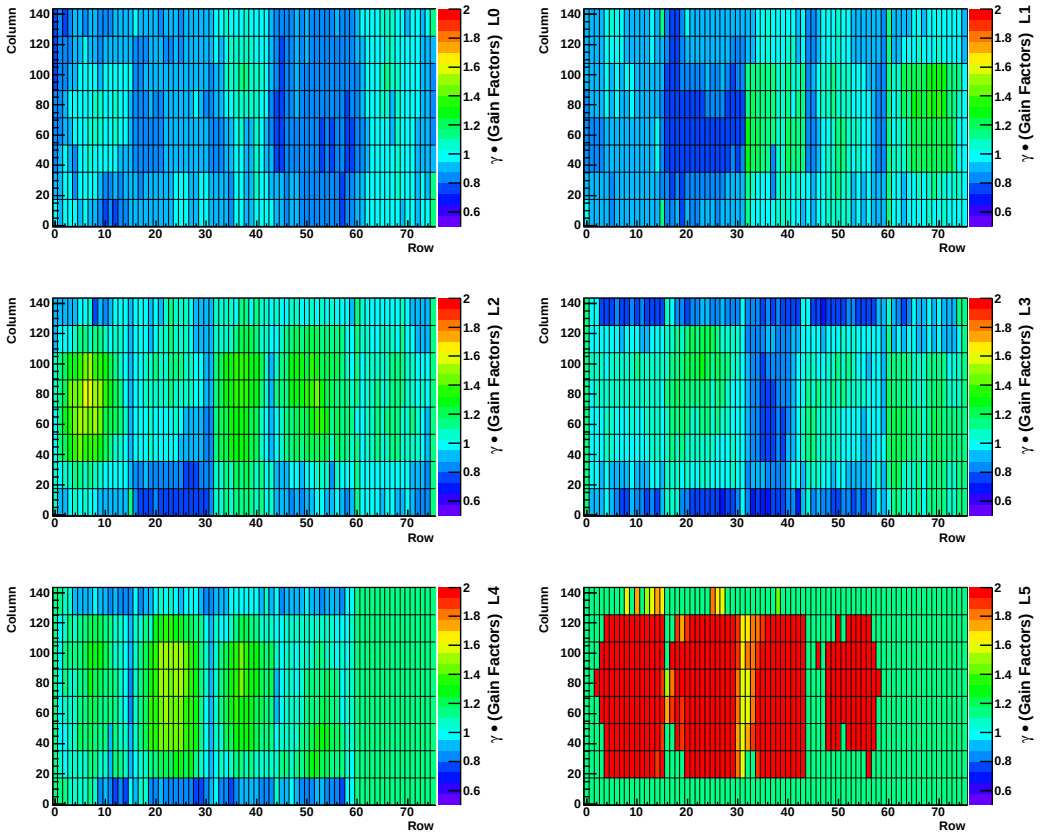

Figure 9.20: Product of gain factors and ADC correction factors for pads in SM-I.

Results of the calculations are given in table 9.3. As should be expected, there are almost no differences between means and standard deviations of gain factors and the products of gain and correction factors of the pads (1). For pads that are placed side by side in column direction and are associated to different MCMs, the standard deviation of steps between $g \cdot \gamma$ is about 3 times higher than for the steps given by different pad gains alone (2). Here, it should be remembered that a (4,5) calibration was performed where Δg already represents the step between means of four adjacent pads in column direction. It can be assumed that the gain distribution will become even flatter for a pad-wise calibration. In row direction (3), differences in standard deviations between Δg and $\Delta(g \cdot \gamma)$ are much smaller. Fortunately, just ADCs of a single MCM are processed for online tracking and position determination, so the rise in steps for gain corrected ADCs in column direction should not have a negative effect on this.

(1)	M_{1a}	1.077	(2)	M_{2a}	-0.005	(3)	M_{3a}	-0.001
	σ_{1a}	0.372		σ_{2a}	0.029		σ_{3a}	0.062
	M_{1b}	1.112		M_{2b}	0.001		M_{3b}	-0.001
	σ_{1b}	0.361		σ_{2b}	0.088		σ_{3b}	0.068

Table 9.3: Differences between means and standard deviations for pads with and without ADC gain correction, calculated for run 2003.

9.3.2.3 Consideration of the FEE Gain

Since signals of ADC channels 0,1 and 20 are not stored in ESD files, the OCDB created with the AliRoot calibration software only contains gain correction factors for ADC channels 2-19, corresponding to the number of readout pads in the TRD. In the analyses above, ADC channels receiving signals from neighbouring MCMs (channels 0, 1 and 20) were calibrated with the gain factors obtained for their partner channels (18, 19 and 2, respectively) on the neighbouring MCMs (see figure 9.17). However, this procedure neglects possible differences in the signal amplification of the front-end electronics, the *FEE gain*.
With the AliRoot class `AliTRDdigitsManager` it is possible to analyze raw-files directly, a reconstruction into ESDs is not necessary. In raw-files, the signals are stored for each *ADC column*, counted from 0 to 167 in the same direction as the 144 pad columns.

When the signal amplitude of two ADC channels receiving data from the same readout pad are compared, the FEE gain correction factor g_{FEE} for the border ADC channel can be determined relative to the other ADC channel. The total gain factor g_{tot} of the ADC channel is now $g_{tot} = g \cdot g_{FEE}$, so in order to create an online gain table, the correction factors γ_0, γ_1 and γ_{20} of an MCM are divided by the associated g_{FEE}. This provides an uniform gain within the MCMs, also for those ADC channels that are not accessible in the reconstructed offline data.
Figure 9.21 shows results obtained from data taken with detector #24 (stack 4, layer 0) of SM-VIII. At the time of the measurement, this SM was still under construction and only layer 0 could be investigated. The top left panel shows the signals of ADC columns 63 vs. 60 in row 8 as an example, for each event the ADC counts were integrated over the time bins. In this example, the gain factor of ADC column 60 (corresponding to pad column 53) can be found in the OCDB. Corresponding graphs were created for all double processed pads of this detector. The baseline of the signals has to be subtracted in order to determine a correct offset. The MCM settings for cosmic runs include zero suppression, i.e. a certain threshold in ADC counts has to be exceeded to trigger an event. Therefore, a noise

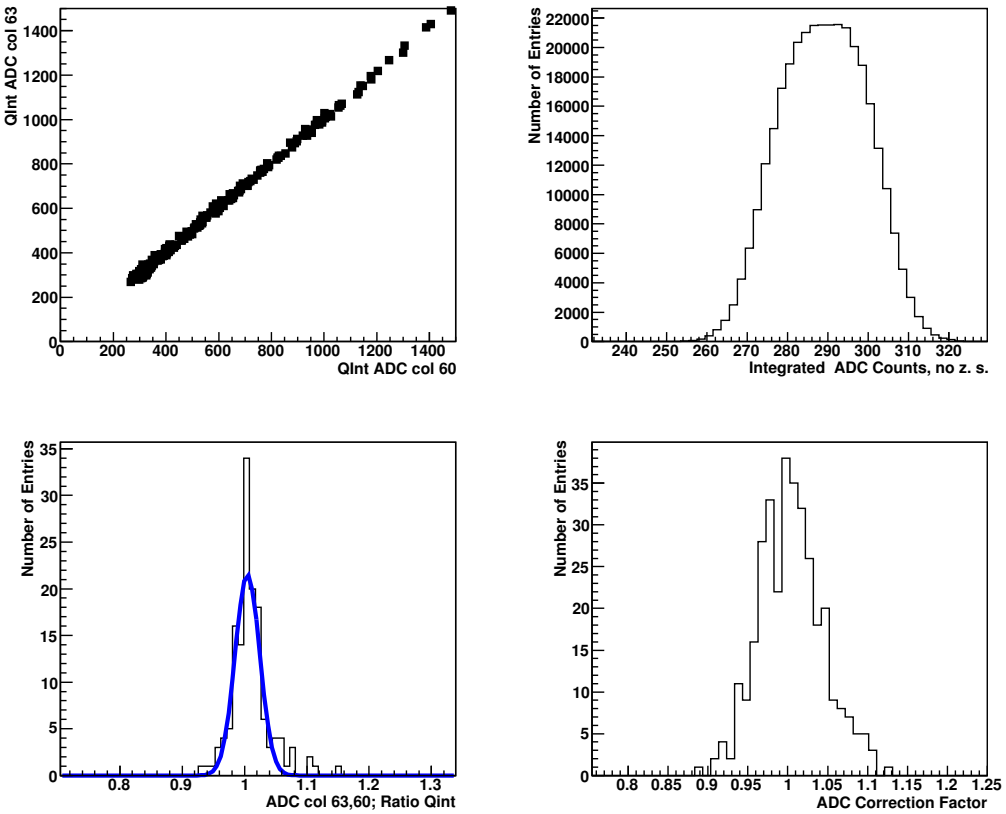

Figure 9.21: Results from the analysis of a cosmic run (2324) and a noise run (2340), both taken with detector #24 of SM-VIII. Top left panel: integrated charge of ADC columns 60 and 63 in row 8, top right panel: distribution of integrated noise in detector #24. Bottom left panel: distribution of noise corrected ratio of integrated charges of ADC columns 60 and 63 in row 8 and Gaussian fit, bottom right panel: distribution of g_{FEE} in detector #24.

run without zero suppression has been taken with detector #24, too. The distribution of the noise is presented in the top right panel of figure 9.21. Again, signals were integrated over the time bins. The mean μ of the distribution is computed as 289.0 with a σ of 10.6. The flattened shape around the mean of the distribution is typical for the MCMs, the origin are uncertainties in the pedestal filter.
The bottom left panel shows the distribution of the ratios of the integrated signals shown in the top left panel corrected for noise, $(Q_{int}(63) - \mu)/(Q_{int}(60) - \mu)$. Only signals with at least 420 ADC counts were analyzed in order to minimize noise effects. The histogram has been fitted with a Gaussian, the mean is taken as g_{FEE} for ADC column 63 in this case.
The bottom right panel presents the distribution of the g_{FEE} factors for detector

#24, each calculated in the same way as described above. The maximum deviation from 1 is approx ±10 %, with a standard deviation of 4 %.

A macro has been written that determines the FEE gain correction factors from two raw-files (one noise and one cosmic run) which stores them into a ROOT file.

9.3.2.4 Adjustment of the MCM Reference Voltage

As mentioned in section 4.6, it is possible to adjust the reference voltage of an MCM in order to achieve a global change in gain for all ADC channels of the MCM. In the FEE, the reference voltage is set by a parameter called *adcdac*, again, this parameter is stored as an integer number with

$$0 \leq adcdac \leq 31\,. \tag{9.8}$$

Usually *adcdac* is set to 0, so the lowest possible reference voltage of 1.05 V is applied to the MCMs, $adcdac = 31$ corresponds to a reference voltage of 1.45 V.

When two ADC channels that process the same pad are compared, it is possible to determine differences in the FEE gain because possible changes in the gas gain apply equally to both ADC channels. With the detector #24 (stack 4, layer 0) of SM-VIII, cosmic runs with different MCM reference voltages were taken. The *adcdac* values of the MCMs 2, 6, 10 and 14 on ROB 2 (located at ROC rows 4 - 7) of this detector were set to 10, 20 and 30. The other MCMs were operated with $adcdac = 0$. Thereby, in this part of the detector the ADC columns 60, 61 and 62 were operated at a different reference voltage than their partner columns 63, 64 and 65. For ADC columns 61 and 62, the FEE gain factors g_{FEE} have been determined in the same way as in the analysis described in the previous section. Let $g_{FEE,0}$ be the FEE gain factor determined from a run with an *adcdac* value of 0 in every MCM and be μ the mean baseline. When the signals of ADC columns 61 and 62 are divided by the associated $g_{FEE,0}$ factors, differences in the ratios of the noise corrected, integrated signals should be determined by differences in the MCM reference voltages. For example, the signal ratios of ADC columns 61 and 64 have been determined in the following way:
Corresponding to the histogram presented in the bottom left panel of figure 9.21, a histogram was filled with the ratios $((Q_{int}(61)/g_{FEE,0,61}) - \mu)/(Q_{int}(64) - \mu)$. Again, the mean of a Gaussian fit was taken as the respective g_{FEE}, or corrected mean signal ratio $< (Q_{int}(61)/Q_{int}(64))_{corr} >$ for the given pair of ADC channels. Only signals with at least 420 ADC counts were analyzed. The results of the measurement are shown in figure 9.22. Each data point represents the mean μ_{row}

of the g_{FEE} over the four rows for a given channel pair and difference in reference voltage. Red dots represent μ_{row} of $g_{FEE,61}$, blue triangles represent μ_{row} of $g_{FEE,62}$. For a better overview, the data points of channel pair (62,65) are displaced by +0.5 bins in x-direction. The errors bars indicate the standard deviation σ of the g_{FEE} of different rows. The σ of the $g_{FEE,62}$ factors from different rows is large compared to the σ of the $g_{FEE,61}$. This is because the $g_{FEE,62}$ factors determined for the channel in row 5 are much lower than those of the other channels, roughly by 10 %. Probably, the FEE gain factor $g_{FEE,0,62}$ computed for this channel is too large, maybe due to low statistics.

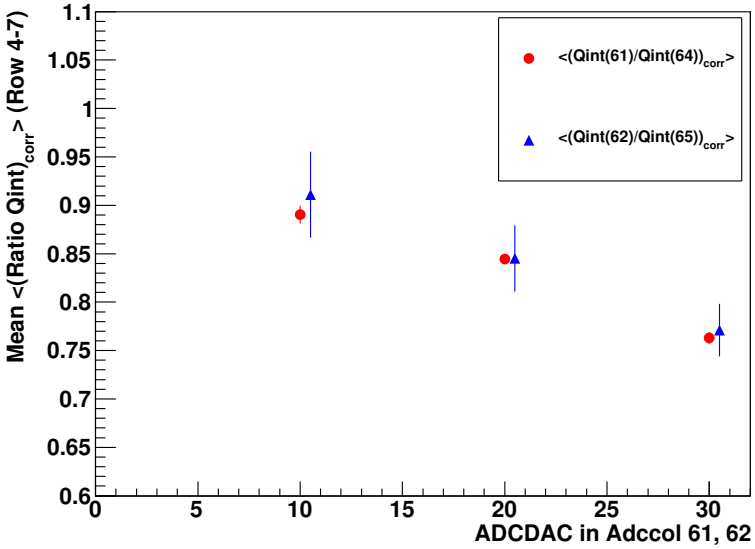

Figure 9.22: Corrected ratios of integrated signals of channel pairs in detector #24 of SM-VIII, given as a mean over 4 rows. The reference voltages of ACD channels 61 and 62 were adjusted. Data points of channel pair (62,65) are displaced by +0.5 in x-direction.

Obviously, the FEE gain decreases with increasing reference voltage. When the signals are compared to a higher reference voltage, the signal amplitudes, thus the FEE gain, decreases. Furthermore, the FEE gain appears to be linearly dependent on the reference voltage. When the decrease in gain is linearly extrapolated over the total range of *adcdac* values, the gain decreases by about 25 %. Relating to an *adcdac* of 16 (corresponding to a reference voltage of about 1.25 V), the FEE gain of an MCM can be adjusted by about ± 15 % via its reference voltage.

9.3.3 Loading of Correction Values into the MCMs

In order to load the correction factors γ and the pedestal additives ϱ into the gain filter stage of the MCMs, as a first step the information is stored in the XML file format. In a second step, the XML file is translated into a binary file. This binary file will be used to store the values into the MCMs. A macro has been written that calculates the correction factors from the gain factors in the OCDB and the FEE gain factors in the ROOT file. Afterwards, it creates the XML file. In figure 9.23, an example of such a file is shown. The file was created with data from run 2003.

First, a name and a description are given. In the file, the biggest blocks are related to the different ROCs. In order to avoid confusions, ROC type and serial number are used for identification. Within a given chamber, the current MCM is determined with the readout board number and a position number. The `adcdac` changes the reference voltage of an MCM (see section 9.3.2.4). Adjusting this value, it might be possible to flatten the gain in the entire TRD and not just within one MCM. On the other hand, this would have negative effects on other detector characteristics (e.g. resolution), so it was decided not to change this value. The `gain` value contains the reciprocal of the mean gain in an MCM in decimal representation, requested for the purpose of online PID. The smallest blocks are the ADCs of the MCMs. The `fgfn` value contains the γ factor, `fgan` contains the pedestal additive.

```
<gaintbl>
  <name>gaintbl_RUN2003_20100121-151713</name>
  <desc>TRD gaintable created on 2010-01-21 15:17:13 by AliRoot
  v4-16-Rev08 with run 2003 and ROCdatabase /home/b_albr01
  /Calibration/01/macros/ROCNb_SMI_TRDSlot2.txt</desc>
  <roc type="L0C1" serial="4">
    <mcm rob="0" pos="0">
      <adcdac>0</adcdac>
      <adc id="0"><fgfn>511</fgfn><fgan>4</fgan></adc>
                            .....
                            .....
      <adc id="19"><fgfn>168</fgfn><fgan>9</fgan></adc>
      <adc id="20"><fgfn>0</fgfn><fgan>0</fgan></adc>
      <gain>1.05902</gain>
    </mcm>
    <mcm rob="0" pos="1">
      <adcdac>0</adcdac>
      <adc id="0"><fgfn>511</fgfn><fgan>4</fgan></adc>
                            .....
                            .....
   </mcm>
  </roc>
  <roc type="L1C1" serial="11">
    <mcm rob="0" pos="0">
      <adcdac>0</adcdac>
      <adc id="0"><fgfn>509</fgfn><fgan>4</fgan></adc>
                            .....
                            .....
                            .....
    </mcm>
  </roc>
</gaintbl>
```

Figure 9.23: Excerpt from the MCM gain table of SM-I, generated with data from runs 2003.

10 Summary

The ALICE experiment at the LHC at CERN is dedicated to explore the QCD phase diagram of nuclear matter. ALICE consists of several detectors, one of them is the Transition Radiation Detector (TRD). The main purpose of the TRD is to distinguish electrons from pions at high p_t. It comprises 540 independent detector modules, composed of a radiator and a time projection chamber with multi-wire proportional readout. The TRD is installed as 18 individual supermodules (SMs), each SM contains 30 readout chambers. The SMs are assembled and tested at the Institute of Nuclear Physics in Münster, where several million tracks of cosmic rays are recorded and reconstructed as part of the assembly process. These tracks can be used to perform a first calibration pass.
In this thesis, the signal amplification, the so-called *gain* of the readout chambers was investigated. In addition, a gain calibration was performed and a method to create a *gain table* containing gain correction factors for each readout channel of the TRD was developed.
The gain was determined with software provided by the official AliRoot framework. This software allows a gain calibration at different granularities of the detector. At the finest granularity, a gain factor is computed for every pad of the TRD, at larger granularities, groups of adjacent pads are summarized in so-called calibration groups. With the data collected in Münster, the finest granularity achieved was 4 pads per calibration group. Furthermore, the software performs a relative gain calibration, i.e. the gain factor for a given calibration group is calculated relative to other parts of the detector, as well as relative to previous calibration passes.
As a first part of the analysis the software was tested. The accuracy of the calculated gain factors decreases with the number of tracklets n found in a calibration group, a function $f(n)$ was found that describes the relative error of the calibration. For 1000 entries, the relative error of a calculated gain factor is around 2 %.
In a good approximation, the gain is exponentially dependent on the anode voltage applied to the readout chambers. Data taken in Münster with SM-VII were fitted with an exponential function, and the relative increase in gain given by an increase of 1 V in anode voltage has been determined to be about 1 %. This result was then compared to previous measurements of the gain in dependence on the anode voltage.

Within the range of their accuracy, all results match with the measurement in this thesis.
When a differential pressure between the gas volume inside the readout chambers and the atmosphere is applied, deformations of the detector modules lead to changes in their gain profiles. In the middle of the chambers, the gain decreases by about 6 % when the differential pressure increases from 0 to +1.2 mbar. Bending of the chambers has a big effect on the shape and height of the gain profiles, it is crucial to keep the differential pressure at a constant level in order to obtain a constant gain.
The TRD can be used as a fast trigger on high p_t electrons. For this purpose a first gain correction has to be performed online in the electronics mounted on the readout chambers. Therefore, the Multi-Chip-Modules (MCMs), the central part of the TRD front-end electronics, provide a gain filter stage.
A long term cosmic run taken with SM-I was analyzed and a macro was developed that computes an online gain table from the gain factors determined with the AliRoot software. Sufficient statistics have to be accumulated in every calibration group in order to obtain reliable gain correction factors. Given the experimental setup in Münster, cosmic ray tracks are very inhomogeneously distributed within the readout chambers. The centres are well filled with tracklets, but the chamber borders are almost never hit by a cosmic ray. The online gain correction is restricted to certain limits, given by the number of binary digits provided by the front-end electronics. When some calibration groups are not well filled with tracklets, gain factors calculated for these groups often exceed the limits. Another difficulty creating an MCM gain table is that the front-end electronics process more readout channels than the offline calibration software. A method was developed to obtain correction factors for these additional channels.

As soon as enough statistics from collision data will be available to perform a pad-by-pad calibration with the SMs already installed at ALICE, online gain correction can be applied.

Bibliography

[A+00] M. C. Abreu et al. Evidence for deconfinement of quarks and gluons from the J/Ψ suppression pattern measured in Pb-Pb collisions at the CERN-SPS. *Physics Letters B*, 477:28–36, 2000.

[A+01] H. K. Ackermann et al. Elliptic flow in Au+Au collisions at $\sqrt{s_{NN}}$ = 130 GeV. *Phys. Rev. Lett.*, 86:402–407, 2001.

[A+02] K. Adcox et al. Flow measurements via two-particle azimuthal correlations in Au+Au collisions at $\sqrt{s_{NN}}$=130 GeV. *Phys. Rev. Lett.*, 89(21):212–301, 2002.

[A+05] K. Adcox et al. Formation of dense partonic matter in relativistic nucleus-nucleus collisions at RHIC: Experimental evaluation by the PHENIX collaboration. *Nuclear Physics A*, 757:184–283, 2005.

[AHR08] M. Appelshäuser, M. Hartig, and P. Reichelt. Measurement of the gas amplification of alice-trd chambers at the ikf. *GSI Scientific Report*, INSTRUMENT-METHODS-50:270, 2008.

[ALI01] ALICE Collaboration, CERN/LHCC2001-021. *ALICE - Technical Design Report of the Transition Radiation Detector*, 2001.

[ALI04] ALICE Collaboration. *ALICE: Physics Performance Report Vol. I + II*, 2004.

[ALI08] ALICE Collaboration. *ALICE - Technical Paper I*, 2008.

[ALI09a] ALICE Collaboration. *http://aliceinfo.cern.ch*, 2009.

[ALI09b] ALICE Collaboration. *http://alien.cern.ch*, 2009.

[And04] A. Andronic. Electron identification performance with ALICE TRD prototypes. *Nucl. Instr. and Meth. A*, 522:40–44, 2004.

[Bai09a] R. Bailhache. *Calibration of the ALICE Transition Radiation Detector and study of Z^0 and heavy quark production in pp collisions at the LHC.* PhD thesis, Technische Universität Darmstadt, 2009.

[Bai09b] R. Bailhache. personal communication, 2009.

[Bat07] B. Bathen. *Aufbau eines Triggers für Tests der ALICE-TRD-Supermodule mit kosmischer Strahlung.* diploma thesis, Westfälische Wilhelms-Universiät Münster, 2007.

[BMS07] P. Braun-Munziger and J. Stachel. The quest for the quark-gluon plasma. *Nature*, 448:302–309, 2007.

[BR94] W. Blum and L. Rolandi. *Particle Detection with Drift Chambers.* Springer, 1994.

[CER95] CERN. *LHC - Conceptional Design.* CERN/AC/95-05(LHC), 1995.

[CER08] CERN. *LHC, the guide*, 2008.

[cer09a] Experiments of the cern heavy ion program. *http:newstate-matter.web.cern.ch*, 2009.

[CER09b] CERN press information. *http://press.web.cern.ch*, 2009.

[Cuv03] J. Cuveland. *Entwicklung der globalen Spurrekonstruktionseinheit für den ALICE-Übergangsstrahlungsdetektor am LHC (CERN).* diploma thesis, Ruprecht-Karls-Universität Heidelberg, 2003.

[eaPDG09] C. Amsler et al. (Particle Data Group). *Physics Letters B*, page 667, 2009.

[Fre05] S. Freuen. *Qualitätstests der ALICE-TRD-Kammern.* diploma thesis, Ruprecht-Karls-Universität Heidelberg, 2005.

[Gri09] H. Grimm. *Entwicklung eines Gassystems zur Ansteuerung, Überwachung und Qualitätskontrolle eines ALICE TRD Supermodules.* diploma thesis, Wesfälische Wilhelms-Universität Münster, 2009.

[Gut02] M. Gutfleisch. *Digitales Frontend und Preprozessor im TRAP1-Chip des TRD-Triggers für das ALICE-Experiment am LHC (CERN).* diploma thesis, Ruprecht-Karls-Universität Heidelberg, 2002.

[Hop04] M. Hoppe. *Aufbau und Inbetriebnahme einer Funkenkammer.* diploma thesis, Wesfälische Wilhelms-Universität Münster, 2004.

[KB09] M. Klein-Bösing. *Development of a Transition Radiation Detector and Reconstruction of Photon Conversions in the CBM Experiment.* PhD thesis, Wesfälische Wilhelms-Universiät Münster, 2009.

[Kle08] Jochen Klein. *Commissioning of and Preparations for Physics with the Transition Radiation Detector in A Large Ion Collider Experiment at CERN.* diploma thesis, Ruprecht-Karls-Universität Heidelberg, 2008.

[L+05] V. Lindenstruth et al. *ALICE TRAP - User Manual*. Universities of Heidelberg, Mannheim, Kaiserslautern, Darmstadt, 2005.

[Meo05] M. Meoni. *Monitoring of a distributed computing system: the Grid AliEn@CERN*. master thesis, University of Florence, 2005.

[Nol05] W. Nolting. *Grundkurs Theoretische Physik 4*, volume 6. Springer, 2005.

[P+06] B. Povh et al. *Teilchen und Kerne*, volume 7. Springer, 2006.

[Rei08] P. Reichelt. *Bestimmung der Gasverstärkung der ALICE-TRD-Auslesekammern*. bachelor thesis, Goethe-Universität Frankfurt, 2008.

[RHI05] RHIC - experimental collaborations, BNL-73847-2005. *Hunting the Quark Gluon Plasma*, 2005.

[Roo09] Root - a data analysis framework. *http://root.cern.ch*, 2009.

[Sau77] F. Sauli. Principles of operation of multiwire proportional and drift chambers. In *Lectures given in the Academic Training Program of CERN 1975-1976*, 1977.

[Sch09] L. Schmoerger. GateDB. *http://alice.uni-hd.de*, 2009.

[Sic09] E. Sicking. *Alignment of ALICE TRD Modules Using Cosmic Ray Data*. diploma thesis, Wesfälische Wilhelms-Universiät Münster, 2009.

[Web96] H. Weber. *2009 at: http://qgp.uni-muenster.de/AGWessels/img/Forschung/*, 1996.

[Wil06] A. Wilk. Analysis of the electron/pion separation capability with real size ALICE TRD prototypes using a neural network algorithm. *Nucl. Instr. and Meth. A*, 563:314–316, 2006.

[WKB09] J. Wessels and C. Klein-Bösing. *Ultrarelativistische Schwerionenphysik: Quarks, Gluonen und Quark-Gluon-Plasma*. lecture, `http://qgp.uni-muenster.de/~jowessel/pages/teaching/ss09/lecture/`, Westfälische Wilhelms-Universität Münster, 2009.

[Wul09] E. S. Wulff. *Position Resolution and Zero Suppresion of the ALICE TRD*. diploma thesis, Wesfälische Wilhelms-Universität Münster, 2009.

[Y+06] W. M. Yao et al. Review of particle physics. *Journal of Physics G: Nucl. and Part. Phys.*, 33:1–1232, 2006.

[YHM05] K. Yagi, T. Hatsuda, and Y. Miake. *Quark-Gluon Plasma*. Cambridge University Press, 2005.

[Zim09] F. Zimmermann. personal communication, 2009.

Danksagung

Abschließend möchte ich mich bei allen Menschen bedanken, die zum Gelingen dieser Arbeit beigetragen haben.

Als erstes danke ich Herrn Prof. Dr. J. P. Wessels für die Aufnahme in die Arbeitsgruppe und die Möglichkeit, spannende Reisen zu den Forschungszentren CERN und GSI zu unternehmen. Vor allem aber möchte ich mich für die Möglichkeit bedanken, als Mitglied einer internationalen Kooperation ein spannendes Thema bearbeiten zu können.

Herrn Prof. Dr. A. Khoukaz danke ich für die Übernahme des Korreferats.

Mein großer Dank gilt Dr. Thomas Dietel für die Betreuung meiner Arbeit und das geduldige Beantworten sehr vieler Fragen. Weiterhin gilt mein großer Dank Dr. Raphaëlle Bailhache für die stete Unterstützung bei der Gain-Kalibration mittels AliRoot.
Für das Korrekturlesen meiner Arbeit danke ich Dr. Thomas Dietel, Dr. Matus Kalisky, Dr. Raphaëlle Bailhache, Bastian Bathen, Dominik Remke, Lars Pfannenschmidt und Max Haardt.
Henriette Gatz und Matthias Walter danke ich für die gute Stimmung im Büro, es hat Spaß gemacht mit euch die Diplomarbeit zu bewältigen.
Für ein tolles Laborklima während des Supermodul-Zusammenbaus danke ich Jonas Anielski, Helmut Baumeister, Bastian Bathen, Ingo Burmeister, Dr. Thomas Dietel, Henriette Gatz, Helge Grimm, Georg Hackmann, Markus Heide, Norbert Heine, Dr. Matus Kalisky, Friederike Poppenborg, Markus Rammler, Eva Sicking, Markus Tegeder, Wolfgang Verhoeven, Matthias Walter, Uwe Westerhoff und Svenja Wulff.

Ich danke der gesamten Arbeitsgruppe für die tolle Arbeitsatmosphäre.

Zuletzt möchte ich mich sehr bei meinen Eltern bedanken, die mir mit ihrem Zuspruch und ihrer finanziellen Unterstützung dieses Studium ermöglicht haben.

Eidesstattliche Erklärung

Ich versichere, dass ich die vorliegende Arbeit selbständig verfasst und keine anderen als die angegebenen Hilfsmittel verwendet habe. Alle Textstellen, die dem Wortlaut oder dem Sinn nach anderen Werken entnommen sind, wurden unter der Angabe der Quelle deutlich gekennzeichnet.

Münster, Februar 2010

.....
(Björn Albrecht)